LIN28B-mediated PI3K/AKT pathway activation promotes metastasis in colorectal cancer models

Authors

Alice E. Shin[1], Kensuke Sugiura[1], Secunda W. Kariuki[1], David A. Cohen[2], Samuel P. Flashner[1], Andres J. Klein-Szanto[3], Noriyuki Nishiwaki[1], Dechokyab De[1], Neil Vasan[4], Joel T. Gabre[1], Christopher J. Lengner[5], Peter A. Sims[6], Anil K. Rustgi[1*]

Affiliations

[1]Herbert Irving Comprehensive Cancer Center, Division of Digestive and Liver Diseases, Department of Medicine, Vagelos College of Physicians and Surgeons, Columbia University Irving Medical Center; New York, NY, USA.

[2]Department of Surgery, Herbert Irving Comprehensive Cancer Center, Vagelos College of Physicians and Surgeons, Columbia University Irving Medical Center; New York, NY, USA.

[3]Histopathology Facility, Fox Chase Cancer Center; Philadelphia, PA, USA.

[4]Division of Hematology and Oncology, Department of Medicine, Herbert Irving Comprehensive Cancer Center, Vagelos College of Physicians and Surgeons, Columbia University Irving Medical Center; New York, NY, USA.

[5]Department of Biomedical Sciences, School of Veterinary Medicine, and Institute for Regenerative Medicine, University of Pennsylvania; Philadelphia, PA, USA.

[6]Department of Systems Biology, Herbert Irving Comprehensive Cancer Center, Vagelos College of Physicians and Surgeons, Columbia University Irving Medical Center; New York, NY, USA.

*Corresponding author:

Anil K. Rustgi, M.D.
Herbert and Florence Irving Professor of Medicine
Director, Herbert Irving Comprehensive Cancer Center
Columbia University Irving Medical Center
Room 201, ICRC
1130 St. Nicholas Avenue
New York, New York 10032
akr2164@cumc.columbia.edu
1-215-771-6361

The authors have declared that no conflict of interest exists.

Abstract

Colorectal cancer (CRC) remains a leading cause of cancer death due to metastatic spread. LIN28B is overexpressed in 30% of CRCs and promotes metastasis, yet its mechanisms remain unclear. In this study, we genetically modified CRC cell lines to overexpress LIN28B, resulting in enhanced PI3K/AKT pathway activation and liver metastasis in mice. We developed genetically modified mouse models with constitutively active *Pik3ca* that form intestinal tumors progressing to liver metastases with an intact immune system, addressing the limitations of previous *Pik3ca*-mutant models, including long tumor latency, mixed histology, and lack of distant metastases. The PI3Kα-specific inhibitor alpelisib reduced migration and invasion in vitro and metastasis in vivo. We present the first comprehensive analysis of vertical inhibition of the PI3K/AKT pathway in CRC using FDA-approved drugs alpelisib and capivasertib (an AKT inhibitor) in combination with LY2584702 (an S6K inhibitor) in CRC cell lines and mouse- and patient-derived organoids (PDOs). Tissue microarrays from CRC patients confirmed that LIN28B and PI3K/AKT pathway activation correlate with CRC progression. These findings highlight the critical role of the LIN28B-mediated PI3K/AKT pathway in CRC metastasis, the therapeutic potential of targeted inhibition, and the promise of PDOs in precision medicine in metastatic CRC.

Brief summary

LIN28B overexpression activates the PI3K/AKT pathway in colorectal cancer, promoting metastasis. Combined vertical inhibition with PI3K pathway-targeting drugs reduces tumor spread.

Keywords

Metastatic colorectal cancer, PI3K/AKT, PIK3CA, alpelisib, capivasertib, LY2584702, cancer metastasis, patient-derived organoids, genetically engineered mouse models.

Main Text

INTRODUCTION

Colorectal cancer (CRC) remains a substantial public health concern in the United States (US) and worldwide. With 1.9 million new cases globally in 2022 and an estimated 150,000 new cases in the US in 2024, CRC is the third most common cancer in the world (1). Localized CRC benefits from effective therapies and has a 5-year survival rate of up to 91%. However, metastatic CRC (mCRC) has a dismal prognosis with a 5-year survival rate of 13% (2). Thus, there is a compelling rationale to unravel the molecular mechanisms underlying mCRC to foster the integration of translational therapeutics.

Classically, CRC has served as a model for understanding the cooperation of oncogenic mutations (e.g., *KRAS*, *BRAF*, *PIK3CA*, and *LIN28B*) and the inactivation of tumor suppressor genes (e.g., *APC*, *TP53*, and *SMAD4*) in fostering primary tumorigenesis (3). Among these, the role of LIN28B has garnered attention as an RNA binding protein influencing gene regulation and cancer progression. The LIN28 proteins (LIN28A and LIN28B) regulate gene expression by binding to messenger RNA post-transcriptionally. The tumor-suppressing microRNA *let-7* is the most well-characterized target of LIN28, but we and others have demonstrated both *let-7* dependent and independent regulation of LIN28 (4-10). While both LIN28A and LIN28B paralogs are critical to various human developmental processes, LIN28B has emerged as a potent oncogene across several cancers (11). LIN28B is overexpressed in esophageal, breast, and prostate cancers and is often an indicator of advanced disease state and poor prognosis (4, 11-13). In CRC, LIN28B is overexpressed in 30% of cases and is associated with poor survival rates and an increased probability of tumor recurrence (12). Additionally, LIN28B overexpression promotes CRC

initiation, progression, and metastasis (4, 5, 12, 14). Despite LIN28B's clear role in inducing tumorigenesis and metastasis, the exact mechanisms through which it exerts these effects remain elusive.

The phosphatidylinositol 3-kinase (PI3K) family of enzymes mediate signals downstream of cell membrane receptors, such as receptor tyrosine kinases [e.g., epidermal growth factor receptor (EGFR) and insulin receptors] and G protein-coupled receptors (15). Class I PI3Ks consist of one catalytic subunit with four isoforms (p110α, p110β, p110γ, and p110δ) that most commonly associate with the p85 regulatory subunit. The resulting heterodimers are termed PI3Kα, PI3Kβ, PI3Kγ, or PI3Kδ, after their respective catalytic subunit (16). Activation of PI3K facilitates downstream signaling primarily through Protein Kinase B (PKB, or AKT) (15). AKT then activates downstream targets to regulate cell survival, proliferation, differentiation, and metabolism (17, 18). Hyperactivation of Class I PI3Ks promotes aberrant cell growth and malignant transformation (15, 19). Additionally, PI3K activation has been suggested to promote metastasis, likely due to its role in epithelial-mesenchymal transition (EMT) and angiogenesis (20-23).

In CRC, PI3K pathway mutations occur in approximately 50-70% of cases, with alterations in the *PIK3CA* gene present in 15-20% of CRC cases, making *PIK3CA* one of the most commonly mutated genes in CRC (24-26). These mutations are typically associated with poor clinical outcomes and reduced efficacy of anti-EGFR monoclonal antibody therapies (27-30). Despite the prevalence of *PIK3CA* mutations, there are currently no US Food and Drug Administration (FDA)-approved therapies targeting *PIK3CA*-mutant mCRC. Furthermore, PI3K inhibitors have shown low response rates as monotherapy in *PIK3CA*-mutant and widely mCRC patients (31, 32), underscoring the need for more effective combination therapeutic strategies. Vertical inhibition of

the PI3K pathway at multiple points (upstream and downstream) using FDA-approved drugs is a promising approach, analogous to the successful BRAF/MEK inhibition in *BRAF*-mutant cancers (33). The recent development of PI3Kα-specific inhibitors, which are less toxic and more specific, enhances the feasibility and effectiveness of combination therapies. (34, 35).

Currently, the primary therapeutic regimen for mCRC includes systemic chemotherapy and targeted therapies that focus on pathways such as EGFR, angiogenesis, and multi-kinase inhibitors. While effective, these traditional chemotherapeutic drugs are DNA-damaging agents and thus affect all rapidly dividing cells, leading to toxicity and limiting their duration. Existing targeted therapies, although more specific, also face challenges such as resistance, toxicity, and limited efficacy in some patients. Given the lethality of mCRC, it is crucial to investigate the mechanisms of metastasis and develop targeted therapies (36).

In this study, we demonstrate that LIN28B expression in CRC cells activates the PI3K/AKT pathway and promotes metastasis to the liver. We developed GEMMs with mutant *Pik3ca* that form primary intestinal tumors within three months, with a subset progressing to liver metastasis, overcoming the limitations of previous models (35, 36). Additionally, we provide a comprehensive analysis of vertical inhibition of PI3Kα, AKT, and ribosomal protein S6 kinase (S6K) using FDA-approved drugs, including alpelisib and capivasertib, in combination with LY2584702, in CRC cell lines and 3D patient-derived organoids (PDOs). Treatment with these inhibitors effectively reduced cell proliferation, migration, invasion, organoid growth, and inhibited liver metastasis formation in vivo. Furthermore, our study demonstrates that PDOs can advance precision medicine in mCRC, as drug responses were dependent on mutational profiles obtained from clinical testing conducted on tumor tissues and whole exome sequencing (WES) of

PDOs. Our findings underscore the critical role of the PI3K/AKT pathway in CRC metastasis and highlight the therapeutic potential of targeting this pathway to manage mCRC.

RESULTS

LIN28B expression in CRC cells activates the PI3K/AKT pathway and promotes liver metastasis

To determine whether LIN28B expression in CRC cells leads to metastasis formation, we generated CRC cells with genetic modification of LIN28B expression as described previously (5, 14). Endogenous LIN28B levels are low in human LoVo and DLD-1 CRC cell lines, which correspondingly exhibit minimal metastatic propensity when injected into the portal vein of immune-compromised mice. Thus, we generated LoVo and DLD-1 cells with LIN28B expression and GFP fluorescence (LIN28B^{high}). The increase in LIN28B protein levels was confirmed via immunoblotting (Figure 1A). These LIN28B^{high} CRC cells were then injected into the portal vein of 6- to 8-week-old Taconic NCr nude mice (*CrTac NCr-Foxn1^{nu}*), and liver tissues were harvested six weeks post-injection (Figure 1B). As anticipated, injection of parental LoVo and DLD-1 cells containing empty vectors (EV) resulted in minimal metastatic formation in the liver, with metastases forming in 1/7 mice (14%) for LoVo cells and none in DLD-1 cells (0/7 mice). Conversely, injections of LoVo LIN28B^{high} and DLD-1 LIN28B^{high} cells led to significantly higher rates of liver metastasis, with metastases occurring in six out of 10 (60%) and eight out of 10 (80%) mice, respectively (Figure 1, C-E). We confirmed that the increased metastatic propensity of LIN28B^{high} cells was not attributable to increased growth or prolonged survival of the 2D cell lines (Supplemental Figure 1A). These results reveal that LIN28B expression in CRC cells enhances their metastatic potential.

To elucidate the downstream signaling pathways activated by LIN28B, we conducted RNA sequencing (RNA-seq) of LIN28B^{high} cells compared to EV cells. Subsequent gene set enrichment

analysis (GSEA) revealed that "MTORC1 signaling" and "PI3K AKT MTOR signaling" hallmark pathways were upregulated in LIN28B^{high} cells (Figure 1F). This was confirmed by Kyoto Encyclopedia of Genes and Genomes (KEGG) analysis of upregulated genes in LIN28B^{high} LoVo and DLD-1 cells compared to their respective EV control cells. By overlapping the upregulated genes between the two cell lines, 2061 common genes were identified and analyzed using KEGG. The “colorectal cancer” pathway was among the significant hits, which included genes involved in the PI3K/AKT pathway (Supplemental Figure 1B). WES further revealed an increased number of mutations in genes within the PI3K/AKT pathway in LIN28B^{high} cells when compared to EV cells (Supplemental Figure 1C).

To confirm the RNA-seq results, we performed immunoblotting to detect phosphorylated AKT (pAKT) (Ser473) levels, a key effector of PI3K/AKT pathway activation. Consistent with our sequencing data, LIN28B^{high} cells exhibited increased pAKT levels compared to EV controls, with no changes in total AKT (tAKT) (Figure 1G). A comprehensive analysis using a PI3K/AKT Pathway Phosphorylation Array showed that LIN28B^{high} cells harbored elevated phosphorylation of several critical proteins within the pathway, including AKT, Bcl-2-associated death promoter (BAD), extracellular signal-regulated kinase 1 and 2 (ERK1/2), glycogen synthase kinase 3-α (GSK3α), p27, p53, S6K, proline-rich Akt substrate of 40 kDa (PRAS40), RAF1, and ribosomal S6 kinase 2 (RSK2) (Figure 1H). Taken together, these data suggest that LIN28B expression in CRC cells activates the PI3K/AKT pathway with concurrent promotion of liver metastasis.

Activation of the PI3K/AKT pathway induces colonic crypt hyperplasia and drives CRC tumorigenesis and metastasis

To validate our hypothesis that the PI3K/AKT pathway acts downstream of LIN28B, we aimed to replicate the metastatic propensity of LIN28B^{high} cells by activating the PI3K/AKT pathway pharmacologically using SC79, a pan-AKT activator. Increasing the concentration of SC79 to 20 μM or higher compromised cell viability in DLD-1 cells, thereby preventing the collection of high-quality proteins for further analysis (Supplemental Figure 2A). This increased sensitivity in DLD-1 cells, which may be attributed to existing *PIK3CA* mutations (unlike in *PIK3CA* wild-type LoVo cells) guided our decision to use 5 μM SC79 for subsequent assays. Immunoblotting confirmed that 5 μM SC79 increased pAKT and phosphorylated ribosomal protein S6 (pRPS6; downstream of S6K) levels in both LoVo and DLD-1 EV cells (Supplemental Figure 2B). Treatment with 5 μM SC79 increased cell migration as observed in the wound healing (scratch) assay (Supplemental Figure 2C) and enhanced invasion capabilities as measured by the QCM ECMatrix Cell Invasion Assay, evaluating the ability of tumor cells to invade through an extracellular matrix (ECM) model (Supplemental Figure 2D).

We next aimed to independently corroborate the metastatic propensity of LIN28B^{high} cells by genetically activating the PI3K/AKT pathway. To achieve this, we generated a *Villin^{Cre};Rosa26^{Pik3ca}* mouse model on a C57BL/6J background. This genetic configuration allows for the induced expression of a constitutively active mouse catalytic P110α subunit of PI3Kα and eGFP in all intestinal and colonic epithelial cells, starting at embryonic day 12.5 (Figure 2A) (37, 38). Colonic crypts were isolated from these mice to culture 3D colonic organoids. Analysis included three genotypes: wild type (*R26$^{WT/WT}$*), heterozygous mutant (*R26$^{Pik3ca/WT}$*), and homozygous mutant (*R26$^{Pik3ca/Pik3ca}$*), with all groups being hemizygous for *Villin^{Cre}*. The mutant organoids were confirmed as GFP positive (Figure 2B) and exhibited increased pAKT levels (Figure 2C). Homozygous mutant organoids demonstrated an increased growth rate (Figure 2D),

and both heterozygous and homozygous mutant organoids showed enhanced organoid formation efficiency, as determined by quantifying the number of organoids formed from an equivalent number of plated crypts on day 3 (Figure 2, B and E). In vivo analyses of the distal to proximal end of the colon showed both GFP expression and elevated pAKT levels in the colonic epithelium of heterozygous and homozygous mutant mice (Figure 2, F and G, Supplemental Figure 2E). Interestingly, these groups also exhibited increased number of cells expressing the marker of proliferation (Ki67) and heightened crypt hyperplasia, marked by increased crypt lengths measured along the distal to proximal colon, indicative of augmented proliferation (Figure 2, F and G, Supplemental Figure 2E).

Longitudinal studies revealed that while $Vil^{Cre};R26^{WT/WT}$ mice remained healthy at 60 weeks of age, $Vil^{Cre};R26^{Pik3ca/WT}$ mice succumbed to tumors between 31 and 43 weeks of age, and $Vil^{Cre};R26^{Pik3ca/Pik3ca}$ mice succumbed to tumors between 16 and 38 weeks of age (Figure 3A). We first confirmed that the mice were not dying due to altered glucose metabolism, considering that the activation of the PI3K/AKT pathway promotes glucose uptake in cells (39). A glucose tolerance test revealed no significant difference between $Vil^{Cre};R26^{WT/WT}$ and $Vil^{Cre};R26^{Pik3ca/Pik3ca}$ mice (Supplemental Figure 3A). $Vil^{Cre};R26^{Pik3ca/Pik3ca}$ mice exhibited a spectrum of neoplastic lesions. In the colon, well-differentiated adenomas confined to the mucosa were observed in 2/9 mice (22%), and moderately-differentiated cancers that penetrated the basement membrane were observed in 1/9 mice (11%) (Figure 3, B-D, Supplemental Figure 3B). In the small intestine (SI), tumors were present in 7/9 mice (78%), with well-differentiated adenomas in 1 mouse (11%) and moderately-differentiated adenocarcinomas in 6/9 mice (67%) (Figure 3, B-D, Supplemental Figure 3B). Additionally, liver metastases were confirmed in 2/9 mice (22%) that also had intestinal adenocarcinomas, as shown by CDX2 (marker of intestinal epithelial cells) and Alcian

blue (highlights mucin production) staining (Figure 3D) (14, 40). This observation was confirmed in *Vil^{CreERT};Rosa26$^{Pik3ca/Pik3ca}$* mice treated with tamoxifen at six weeks of age, which is an inducible model for temporal regulation of mutant *Pik3ca* expression (41). Two of five mice (40%) developed moderately-differentiated colonic cancers, 3/5 (60%) mice developed moderately differentiated SI cancers, and 1/5 (20%) mice developed a well-differentiated SI adenoma. However, these mice did not have liver metastases by 21-40 weeks of age (Figure 3A-C, Supplemental Figure 3B).

To further explore the effects of PI3Kα activation on colorectal metastasis, we utilized a well-established carcinogen-induced sporadic mouse model of CRC. Injections of 10 mg/kg azoxymethane (AOM) every week for six weeks have been reported to lead to well-differentiated colonic adenomas that remain confined to the basement membrane in wild-type C57BL/6J mice, with minimal effects on the SI or the liver (42-44). *Villin^{Cre};Rosa26^{Pik3ca}* mice were injected with AOM, and tissues from *R26$^{WT/WT}$* mice were harvested at 30 weeks post first injection of AOM for analysis (Supplemental Figure 3C). *R26$^{Pik3ca/WT}$* and *R26$^{Pik3ca/Pik3ca}$* mice had to be euthanized when they exhibited signs of severe illness, such as substantial weight loss or a severely deteriorated condition (Figure 3E, Supplemental Figure 3, C and D). Administering tamoxifen at nine weeks post first injection of AOM to *Villin^{CreERT};R26^{Pik3ca}* mice enabled temporal control of mutant PI3Kα expression after primary colonic tumor formation, allowing focused analysis on the effects of active PI3Kα on metastatic progression (Supplemental Figure 3C). Survival curves highlight reduced lifespans in both heterozygous and homozygous *R26^{Pik3ca}* mutant mice using either *Vil^{Cre}* or *Vil^{CreERT}* alleles (Figure 3E). Histological assessments revealed well-differentiated colonic adenomas in *R26$^{WT/WT}$* mice treated with AOM, with adenomas detected in 5/6 (83%) *Vil^{Cre}* and 6/12 (50%) *Vil^{CreERT}* mice. By contrast, a subset of *R26^{Pik3ca}* mutant mice developed moderately-

differentiated colonic adenocarcinomas (Figure 3, F-H, Supplemental Figure 3, E and F). Additionally, the majority of *R26*^{Pik3ca} mutant mice developed SI adenocarcinomas localized primarily in the duodenum and jejunum (Figure 3, F-H, Supplemental Figure 3, E and F). Remarkably, *R26*^{Pik3ca} mutant mice developed metastases in the liver, as observed in 4/27 (14.8%) *Vil*^{Cre} and 6/20 (30%) *Vil*^{CreERT} mice (Figure 3, F-H, Supplemental Figure 3, E and F). We confirmed that the liver metastases originated from primary intestinal tumors by CDX2 staining (Supplemental Figure 3G). It is conceivable that penetrance of primary tumors and liver metastasis would be greater if mice lived longer, especially in the case of *Vil*^{Cre}*;R26*^{Pik3ca} mice; however, this was mitigated by deteriorated condition of the mice that prompted euthanasia at the specified time points, most likely due to tumor-induced obstruction. Other organs, including the lung, pancreas, and thymus, remained unaffected, suggesting metastatic tropism to the liver. Collectively, our data demonstrate that genetic activation of the PI3K/AKT pathway promotes primary tumorigenesis and liver metastasis in our mouse models.

Alpelisib impairs LIN28B-induced cell migration and invasion and inhibits PI3Kα-induced organoid growth

Having established the role of PI3Kα activation in CRC metastasis in vivo, we next assessed the therapeutic potential of inhibiting PI3Kα to inhibit metastatic progression. To date, such a therapeutic approach has not been pursued for FDA approval, affording new perspectives in mCRC (36). For this purpose, we used alpelisib, a PI3Kα-specific inhibitor currently approved by the FDA for treating hormone receptor (*HR*)-positive, human epidermal growth factor receptor 2 (*HER2*)-negative, *PIK3CA*-mutated advanced or metastatic breast cancer (45).

A viability assay revealed that cell viability began to decrease at concentrations starting from 10 μM of alpelisib in LoVo and DLD-1 cell lines but does not decrease at 5 μM (Supplemental Figure 4, A and B). Immunoblot analysis showed that LIN28B^{high} cells exhibited elevated pAKT levels compared to EV cells, and treatment with 5 μM and 10 μM alpelisib reduced pAKT levels in LIN28B^{high} cells to those comparable with EV cells, indicating effective pathway inhibition (Figure 4A). Based on this, we selected 5 μM for subsequent experiments, as this concentration does not reduce the viability of any of the cell lines used (Supplemental Figure 4C). A soft agar colony formation assay, which assesses anchorage-independent growth, revealed that LIN28B^{high} cells treated with 5 μM alpelisib exhibited reduced colony formation, reverting to control levels observed in EV cells (Figure 4B). A wound healing assay revealed that treatment with 5 μM alpelisib reduced cell migration at 36- and 48-hours post-treatment in LIN28B^{high} cells, with a notable effect also observed in EV cells at 48 hours (Figure 4C). The QCM ECMatrix Cell Invasion Assay showed that alpelisib had no effect on EV cells but reduced the number of invading LIN28B^{high} cells at both 5 μM and 10 μM, demonstrating alpelisib's potent anti-invasion effects (Figure 4D).

We next tested the effects of alpelisib using colonic organoids derived from *Villin^{Cre};Rosa26^{Pik3ca}* mice (Figure 4E). Organoids from all three genotypes (*R26$^{WT/WT}$*, *R26$^{Pik3ca/WT}$*, and *R26$^{Pik3ca/Pik3ca}$*) were treated with 5 μM alpelisib. Immunoblotting demonstrated decreased pAKT (Ser473) in *R26$^{Pik3ca/WT}$* and *R26$^{Pik3ca/Pik3ca}$* organoids, corroborating the inhibitor's efficacy (Figure 4F). Alpelisib significantly reduced organoid growth in both *R26$^{Pik3ca/WT}$* and *R26$^{Pik3ca/Pik3ca}$* organoids, with no discernible effect on *R26$^{WT/WT}$* organoids (Figure 4G). These results indicate that alpelisib impairs LIN28B-induced cell proliferation, migration, and invasion and inhibits PI3Kα-induced organoid growth.

Alpelisib inhibits colorectal liver metastasis formation in mice

To investigate the in vivo effects of alpelisib on CRC metastasis, we employed the mCRC portal vein injection model. LIN28B^{high} CRC cells were injected into the portal vein of NCr nude mice. Two weeks post-injection, mice were administered oral gavage of 25 μg/g alpelisib every two days for a period of four weeks, after which the livers were harvested for analysis (Figure 5, A and B) (46). Mice treated with alpelisib appeared healthier and exhibited less weight loss compared to the vehicle-treated control group, suggesting improved general health, although the difference was not statistically significant due to variability within the vehicle-treated group (Figure 5C). No changes were observed in liver weight, indicating that alpelisib did not adversely affect liver mass (Figure 5D). Treatment with alpelisib resulted in a significant reduction of liver metastases derived from LIN28B^{high} CRC cells, with only 1/10 (10%) of alpelisib-treated mice developing a micrometastasis, highlighting the efficacy of alpelisib in inhibiting metastatic progression (Figure 5, B, E, and F).

To confirm these findings, we employed the transgenic *Vil*^{CreERT}*;R26*$^{Pik3ca/Pik3ca}$ model of mCRC. These mice were treated with AOM and tamoxifen, followed by 25 μg/g alpelisib administration every two days (Figure 5G). Alpelisib treatment inhibited liver metastasis formation, as observed by gross inspection and confirmed through histological analysis of serial liver sections (Figure 5, H and I). These findings underscore the potential of alpelisib to inhibit liver metastasis formation in two independent mouse models of mCRC.

Pharmacologic inhibition of the S6K/RPS6 axis suppresses LIN28B-driven cell migration and invasion in CRC cells

To elucidate the downstream effects of PI3Kα inhibition by alpelisib, we conducted RNA-seq of LIN28B^{high} CRC cells, untreated and treated with alpelisib. GSEA identified "MTORC1 signaling" as a top hallmark pathway that was enriched in vehicle-treated cells compared to alpelisib-treated cells (Figure 6A). Consistent with this finding, we analyzed a published dataset (GSE50760) which involved RNA-seq of samples from primary CRC and matched liver metastases from 18 CRC patients (47). "MTORC1 signaling" was enriched in the matched liver metastases relative to primary tumors (Figure 6B), prompting us to further investigate MTORC1 signaling downstream of the PI3K/AKT pathway with and without alpelisib treatment.

The PI3K/AKT Pathway Phosphorylation Array showed that levels of pAKT, pS6K (downstream of MTORC1), and pRPS6 (downstream of S6K) in LIN28B^{high} cells were reduced to levels comparable to EV when treated with alpelisib (Figure 6C), suggesting that while LIN28B expression increases MTORC1 signaling, alpelisib can effectively reverse this effect. However, mTOR phosphorylation was not significantly reduced by alpelisib treatment, likely due to PI3K-independent mechanisms regulating mTOR activation (48, 49). This observation was corroborated by immunoblotting, which showed decreased levels of pS6K and pRPS6 upon alpelisib treatment in LIN28B^{high} CRC cells (Figure 6D). Staining of the colonic tissues from *Villin^{Cre};Rosa26^{Pik3ca}* mice confirmed increased staining of pS6K and pRPS6 in both *R26$^{Pik3ca/WT}$* and *R26$^{Pik3ca/Pik3ca}$* mouse models (Figure 6E, Supplemental Figure 5).

Given these findings, we explored the potential additive effects of inhibiting S6K activation in combination with alpelisib. LY2584702, a selective ATP-competitive S6K inhibitor, was tested at concentrations of 1, 5, and 10 μM on both EV and LIN28B^{high} CRC cells. Concentrations of 1,

5, and 10 μM of LY2584702 reduced pRPS6 levels in EV and LIN28B^{high} cells without inducing cytotoxicity (Figure 6F, Supplemental Figure 4, A and B). A wound healing assay demonstrated that either 5 μM alpelisib or 5 μM LY2584702 reduced cell migration in LIN28B^{high} cells at 48 or 72 hours when compared to the vehicle-treated control group, respectively (Figure 6G). When LY2584702 was combined with alpelisib, there was a greater effect in reducing wound healing, indicating an additive effect (Figure 6G). The QCM ECMatrix Cell Invasion Assay revealed a decreased ability of LIN28B^{high} CRC cells to invade through the ECM with treatments of alpelisib or LY2584702. The combination treatment with alpelisib and LY2584702, although not statistically significant when compared to single treatment groups, showed a trend towards decreased invasion (Figure 6H). Collectively, these results demonstrate that pharmacologic inhibition of the S6K/RPS6 axis using LY2584702 suppresses LIN28B-driven cell migration and invasion in CRC cells, and combining PI3Kα inhibition with S6K inhibition may have an additive effect.

Pharmacologic inhibition of PI3Kα and S6K impairs the growth of patient-derived CRC organoids

Next, we established 3D PDOs from primary CRC tumors (Table 1). Surgical specimens of colonic tumors were collected, and cells were isolated and cultured in Matrigel. Notably, the organoids designated as CRC28 were derived from a patient whose liver metastasis was resected concurrently, providing a unique opportunity to establish a matched liver metastasis organoid line ("CRC28met"). Histological examination confirmed the tumor status (differentiation and stage) of each sample, alongside its adjacent normal colon tissue and liver metastasis in the case of CRC28 (Supplemental Figure 6A). Prior to organoid culture, tumor samples were analyzed for mutations

in genes known to impact clinical management via the Columbia Solid Tumor Panel (CSTP) specific for colorectal and pancreatic cancers (Table 2). Interestingly, 4/5 samples (80%) with *PIK3CA* mutations exhibited concurrent *KRAS* mutations, while the remaining sample had a *BRAF* mutation. To understand this observation further, we analyzed data from The Cancer Genome Atlas (TCGA) PanCancer Atlas, which confirmed a significant co-occurrence of *KRAS* and *PIK3CA* mutations in CRC (Supplemental Figure 6B).

Following PDO establishment, WES was performed to verify mutations identified by the CSTP and to discover potential additional mutations. Each organoid line displayed unique mutational profiles (Figure 7A). Interestingly, we observed mutations in one or more genes of the PI3K/AKT pathway in each organoid line (Figure 7B). Specifically, CRC27T, CRC34T, CRC28T, and CRC28met harbored missense mutations in the *PIK3CA* gene (Figure 7B). Additionally, CRC28T and CRC28met displayed distinct mutational profiles. The differences between CRC28T and CRC28met were further analyzed using g:Profiler for biological pathway enrichment (KEGG, Reactome, WikiPathways) (Supplemental Figure 6, C and D). Immunoblotting for pAKT, pMTOR, and pRPS6 demonstrated elevated pathway activity in PDO lines with *PIK3CA* and/or *KRAS* mutations (Figure 7C).

We next evaluated the efficacy of targeted therapeutic agents in these models. The PDOs were treated with alpelisib and LY2584702 to dissect the functional consequences of PI3Kα and S6K inhibition in CRC. To validate these findings and explore the broader clinical applicability of PI3K/AKT pathway inhibition, we included capivasertib, a pan-AKT inhibitor recently approved by the FDA for use in *HR*-positive, *HER2*-negative locally advanced or metastatic breast cancer with *PIK3CA*, *AKT1*, or *PTEN* mutations (50). PDOs with no mutations in clinically actionable genes according to the CSTP (CRC10T, CRC14T, CRC23T) were highly sensitive to alpelisib or

capivasertib as monotherapies. In these lines, LY2584702 alone did not significantly affect organoid growth. However, in the CRC14T and CRC23T lines, the combination of either alpelisib or capivasertib with LY2584702 enhanced the suppression of organoid growth (Figure 7, D and E, Supplemental Figure 7). For organoids with *KRAS* mutations (CRC30T, CRC32T, CRC36T), the effects of the treatments varied and did not exhibit consistent patterns. Alpelisib effectively suppressed growth in CRC32T and CRC36T. However, in CRC32T, LY2584702 paradoxically increased growth, and its combination with alpelisib neutralized alpelisib's effect. Capivasertib was ineffective in both lines. CRC30T showed no significant response to any treatment (Figure 7, D and E, Supplemental Figure 7). Organoids with both *PIK3CA* and *KRAS* mutations (CRC27T, CRC34T, CRC28T, CRC28met) were highly sensitive to either alpelisib or capivasertib as monotherapies (Figure 7, D and E, Supplemental Figure 7). This suggests that the presence of a *PIK3CA* mutation makes organoids more amenable to targeted treatments compared to having a *KRAS* mutation alone. In CRC27T and CRC28met organoid lines, the combination with LY2584702 further enhanced the suppression of organoid growth (Figure 7, D and E, Supplemental Figure 7). The growth suppressing effects of alpelisib or capivasertib in combination with LY2584702 were confirmed in organoids derived from the colonic tumors of $Vil^{Cre};R26^{Pik3ca/Pik3ca}$ mice (Supplemental Figures 8 and 9). Collectively, the ability to pharmacologically inhibit the PI3K/AKT pathway in *PIK3CA*-mutant PDOs underscores the potential of these inhibitors in combination therapies for primary and mCRC, especially in tumors with concurrent *PIK3CA* and *KRAS* mutations.

PI3K-S6K signaling correlates with disease progression in CRC patient samples

To validate our experimental findings and their relevance to clinical progression, we constructed a tissue microarray (TMA) from samples obtained from 60 CRC patients. Each TMA core included tissue from adjacent normal colonic tissue, primary colonic tumors, and liver metastases from the same patients. IHC analysis revealed that 100% of primary colonic tumors and liver metastases were positively stained for LIN28B (Figure 8, A and B, Supplemental Figure 10). We previously reported that 30% of CRCs express LIN28B (12); this discrepancy is likely because the TMAs were constructed from patients who had already developed liver metastases. Additionally, elevated pAKT and pS6K levels were observed in both the primary CRC and matched liver metastases when compared to the adjacent normal tissues (Figure 8, A and B, Supplemental Figure 10). Interestingly, the expression of pRPS6, a downstream effector of both AKT and S6K, was increased in primary tumors compared to adjacent normal tissues, and further elevated in liver metastases compared to the primary tumors (Figure 8, A and B, Supplemental Figure 10). These findings are supported by single cell RNA-sequencing (scRNA-seq) data retrieved from the Human Colon Cancer Atlas (c295), which reveals higher expression of *PIK3CA*, *MTOR*, and *RPS6KB1* in tumor cells compared to healthy cells (Figure 8, C and D, Supplemental Figure 11). Notably, within the tumor cell population, stem/transit amplifying-like cells show enhanced levels of these genes (Figure 8, C and D, Supplemental Figure 11). Taken together, the data from TMA IHC and scRNA-seq suggest that the PI3K signaling pathway, particularly marked by the elevation of pRPS6, correlate with disease progression in CRC patient samples.

DISCUSSION

In this study, we provide insights into CRC pathogenesis by demonstrating that LIN28B expression in CRC cells activates the PI3K/AKT pathway, enhancing their metastatic potential to the liver. Our findings highlight that this metastatic process is dependent upon the activation of the PI3K/AKT pathway within the CRC cells. Pharmacologic and genetic activation of the PI3K/AKT pathway independently corroborated these findings, showing enhanced cell migration, invasion, primary tumorigenesis, and metastasis. Furthermore, we introduce the first GEMM that develops colonic tumors progressing to liver metastases within an intact immune system, driven by a single oncogenic mutation, *Pik3ca*. Importantly, treatment with the pathway inhibitors (alpelisib, capivasertib, and LY2584702) effectively reduced cell proliferation, migration, invasion, and organoid growth, and inhibited liver metastasis formation in vivo.

Our study presents a transgenic mouse model that develops primary intestinal tumors and metastasizes to the liver within an intact immune system, driven by a single oncogenic event, *Pik3ca*, in combination with AOM treatment (51). Previously developed GEMMs of mCRC have typically required multiple oncogenic hits or surgical interventions to achieve similar outcomes. For instance, a GEMM of mCRC involved a surgical procedure to limit adeno-cre infection to the distal colon with homozygous *Apc* conditional knockout and heterozygous for a latent activated allele of *Kras*. This model resulted in liver metastases in 20% of mice within 24 weeks after adeno-cre injection (52). The iKAP mouse model generated by Boutin *et al*. eliminated the need for surgery by using direct 4-OH-tamoxifen enema to $Villin^{CreERT}$ mice with $Apc^{fl/fl}$, $Tp53^{fl/fl}$, and a Tet-inducible $Kras^{G12D}$ allele. This model displayed metastases to the liver and lung within six weeks in 25% of the mice (53). Similar to our approach, others have also combined GEMMs with AOM treatment to induce CRC metastasis in mice. $Villin^{Cre};Trp53^{fl/fl};Akt^{E17K}$ mice develop invasive

tumors and lymph node metastasis (20-30% incidence) when treated with AOM, with tumors closely resembling human CMS4 subtype profiles (54). Additionally, *Villin*^{Cre}*;Trp53*$^{fl/fl}$ mice treated with AOM develop high-grade adenocarcinomas and lymph node metastases (20-30% incidence), but none to the liver or lungs (55). Another commonly used mCRC model involves the orthotopic injection of CRISPR-Cas9-engineered organoids with CRC driver mutations *Kras*^{G12D} and *Trp53*$^{fl/fl}$. However, this model requires dextran sodium sulfate (DSS)-induced inflammation prior to implantation to promote the development of a metastatic phenotype (56). mCRC has also been generated by orthotopic injection of organoids with mutations in *Apc*, *Trp53*, *Kras*^{G12D}, and *Smad4* (57).

In the broader context of PI3K research, our transgenic mouse model addresses limitations observed in existing GEMMs with *Pik3ca* mutations across various cancer types, including breast cancer. Previous GEMMs with *Pik3ca* mutations often exhibit long tumor latency times, sometimes taking more than a year for tumor growth (58). Additionally, these models frequently develop sarcomas rather than adenocarcinomas, the latter of which are the most common *PIK3CA*-mutant tumor types in patients (59). Moreover, existing models have inconsistent tumor formation, lack of metastatic potential, and are often generated in immunocompromised mice, limiting the relevance to human disease (60, 61). Our model overcomes these limitations with genetic evidence of primary intestinal tumors within approximately three months, with some tumors progressing to liver metastases, all achieved within an intact immune system. The histology of the tumors in our model closely resembles the colon adenocarcinoma phenotype observed in patients, providing a more accurate representation of *PIK3CA*-driven colon cancers. This notable advance allows for a more precise study of the PI3K pathway's role in tumor progression and metastasis, offering a valuable platform. The ability of our model to generate tumors rapidly and with appropriate

histological characteristics highlights its potential to impact preclinical research and therapeutic development for PI3K-mutant CRC.

The use of PDOs provided a highly relevant model system that recapitulates the genetic, phenotypic, and histological features of original tumors. Vlachogiannis *et al*. demonstrated the value of PDOs in predicting clinical outcomes in patients with metastatic pre-treated colorectal and gastroesophageal cancers. Their study found that PDOs had a high degree of similarity to patients' tumors and accurately predicted clinical responses to targeted agents or chemotherapy with a sensitivity of 100%, specificity of 93%, positive predictive value of 88%, and negative predictive value of 100% (62). In our study, PDOs enabled us to evaluate the efficacy of PI3K/AKT pathway inhibitors in a model that closely mimics human CRC, thereby providing insights into potential therapeutic strategies.

WES of PDOs from matched primary tumors and liver metastases revealed 1070 genes that were mutated in both primary and metastatic organoids. 122 genes were mutated exclusively in the metastatic organoids (11.4%), while 115 genes were mutated exclusively in the primary organoids (10.7%). The majority of mutant genes overlapped between the two, aligning with previous findings that mCRC genomes are not fundamentally different from primary CRCs in terms of the mutational landscape or the genes driving tumorigenesis (63-65). Genes mutated in metastases predominantly involve immune suppression, EMT, and angiogenesis (63), as well as MYC signaling, DNA repair, glycolysis, metabolic processes, and targets of hypoxia-inducible factor (66). Our analysis revealed pathways such as cAMP and MAPK signaling, ECM degradation, GPCR signaling, MMP activation, and VEGFA-VEGFR2 signaling among the genes mutated exclusively in PDOs derived from metastasis. The overlap of mutated genes between primary tumors and metastases suggests that metastatic potential may be predetermined early in

tumorigenesis, with metastasis-initiating cells already present among the initial cell clones in the primary tumor (36, 67).

It is notable that 80% of tumor tissues collected to generate PDOs with *PIK3CA* mutations also harbored *KRAS* mutations. This was corroborated by TCGA analysis showing high co-occurrence of *PIK3CA* and *KRAS* mutations in CRC, indicating a synergistic or linked pathway involvement. A study evaluating 504 patients with diverse cancers found that *KRAS* mutations were present in 38% of patients with *PIK3CA* mutations compared to 16% of patients with wild-type *PIK3CA* ($p = 0.001$) (68). Specifically in CRC, the analysis of 83 patients with paired primary tumors and matched metastases revealed that 25% of the tumors with mutant *KRAS* and 4% of wild-type *KRAS* tumors had *PIK3CA* mutations ($p = 0.008$) (69). Furthermore, a study of 655 CRC patients found that *KRAS* and *PIK3CA* co-mutations were associated with aggressive clinicopathological features. Patients with both mutations had poorer overall survival compared to those with only one or neither mutation, emphasizing that the concomitant mutation statuses of *KRAS* and *PIK3CA* should be considered for prognostic evaluations in CRC patients (70). Collectively, the co-occurrence of *PIK3CA* and *KRAS* has implications for targeted therapies, as treatments targeting *PIK3CA*-mutant CRC must also be effective against tumors harboring both *PIK3CA* and *KRAS* mutations to achieve optimal therapeutic outcomes.

The differential sensitivity for PI3K pathway inhibitors observed in PDOs based on their mutational status underscores the importance of considering mutational profiling when selecting targeted therapies for CRC. Organoids without clinically actionable mutations were highly responsive to alpelisib or capivasertib. By contrast, organoids with *KRAS* mutations exhibited variable treatment responses, highlighting the complexity of targeting this subgroup. Notably, organoids harboring both *PIK3CA* and *KRAS* mutations were consistently more sensitive to these

targeted therapies. This suggests that *PIK3CA* mutations could serve as predictive markers for treatment efficacy in *KRAS*-mutant CRCs. This is particularly important given that *KRAS* mutations are present in up to 50% of CRC cases and co-occur with *PIK3CA* mutations (71).

It is important to note that several PI3Kδ inhibitors, such as idelalisib, copanlisib, duvelisib, and umbralisib, have been withdrawn from clinical use by the FDA due to immune-related side effects and, in some trials, a reduction in overall survival (59). In contrast, PI3Kα inhibitors such as alpelisib (45) and inavolisib (72), as well as the AKT inhibitor capivasertib (50), remain in clinical use for specific cancer types, with ongoing efforts to mitigate side effects, such as hyperglycemia, through the development of mutant-selective inhibitors like STX-478 (35) and RLY-2608 (34). Moreover, ongoing clinical trials for alpelisib and capivasertib are exploring their efficacy in various cancers, including CRC. Alpelisib, already FDA-approved for *HR*-positive, *HER2*-negative, *PIK3CA*-mutated advanced or metastatic breast cancer (45), is being tested in head and neck squamous cell carcinoma, melanoma, multiple myeloma, gastric cancer, pancreatic cancer, and ovarian cancer. Two clinical trials are investigating alpelisib in CRC. The first is a Phase Ib/II multi-center study of encorafenib (BRAF inhibitor) and cetuximab (EGFR inhibitor) or encorafenib, cetuximab, and alpelisib in patients with *BRAF*-mutant mCRC (NCT01719380). This study, completed in October 2015, indicated that the combination therapies with alpelisib were generally well-tolerated and recommended further evaluation of their efficacy in CRC treatment. The second Phase 1b pharmacokinetics study is an active study assessing the efficacy and safety of alpelisib and capecitabine (chemotherapy) in patients with mCRC who have a *PIK3CA* mutation (NCT04753203). Capivasertib is being investigated in clinical trials for triple-negative breast cancer, B-cell non-Hodgkin lymphoma, and prostate cancer. The only ongoing clinical trial examining capivasertib in CRC is the MATCH Screening Trial (NCT02465060), a

Phase II study evaluating the effectiveness of treatments directed by genetic testing in patients with advanced, refractory solid tumors, lymphomas, or multiple myelomas. Patients with *AKT* mutations will be assigned to capivasertib, while taselisib and copanlisib will target *PIK3CA* or *PTEN* mutant cancers.

The safety profile of LY2584702 has been evaluated in four Phase I clinical trials, yielding divergent results (73, 74). These studies, however, did not incorporate genetic testing as their selection criteria. Our data using PDOs suggest that LY2584702 could be effective when used in combination with PI3K or AKT inhibitors, particularly in patients with both *PIK3CA* and *KRAS* mutations. Organoids that responded well to LY2584702 combined with either alpelisib or capivasertib were derived from patients with either no clinically actionable CRC-related mutations or patients with both *KRAS* and *PIK3CA* mutations. Genetic testing and combination therapy could potentially lower the required dose for efficacy to mitigate the toxicity of LY2584702 observed at higher doses. Further studies are needed to explore the efficacy of LY2584702 in combination with PI3K pathway inhibitors and to determine its potential in clinical settings, particularly in patients with specific genetic backgrounds.

This study is highly relevant and timely given the recent advancements in developing PI3K inhibitors that are less toxic and more specific, making combination therapies more feasible. For example, RLY-2608 selectively inhibits mutant PI3Kα, reducing the risk of side effects associated with wild-type PI3Kα inhibition, such as hyperglycemia, rash, or diarrhea. This drug has shown a partial response in a breast cancer patient with 12 prior lines of therapy and initial anti-tumor activity across a range of doses in breast cancer patients (34). Another promising example is STX-478, an allosteric, mutant-selective PI3Kα inhibitor that interacts with a previously undescribed allosteric pocket within PI3Kα. STX-478 selectively targets mutant PI3Kα, reducing toxicity and

improving efficacy compared to alpelisib. STX-478 avoids metabolic dysfunction, such as hyperglycemia. It has demonstrated robust efficacy in human tumor xenografts, and combining STX-478 with other treatments such as fulvestrant and CDK4/6 inhibitors has provided durable tumor regression without substantial side effects (35).

This study's impact is highlighted by our investigation into vertical inhibition of the PI3K pathway. Vertical inhibition, which involves targeting both upstream and downstream components of the same pathway, has shown promise in therapeutic interventions, analogous to the successful BRAF/MEK inhibition strategy in BRAF mutant cancers (75-77). Our findings demonstrate the effectiveness of vertical inhibition of the PI3K pathway in *PIK3CA*-mutant CRC, providing a promising approach for more effective and safer therapeutic intervention in mCRC, a field bereft of meaningful impact upon 5-year survival rates. It is critical that potential treatments for mCRC pivot on new mechanistic insights, and in this context, we nominate the PI3K pathway as a promising therapeutic target.

Collectively, our study provides insights into the mechanism by which LIN28B mediates CRC metastasis, employing a wide range of models (cell lines, GEMMs, 3D PDOs, and human CRC TMAs) to investigate both the activation and inhibition of the PI3K/AKT pathway downstream of LIN28B. Our findings strongly support the critical role of the PI3K/AKT pathway in CRC metastasis and highlight the therapeutic potential of targeting this pathway.

MATERIALS AND METHODS

Sex as a biological variable

Both female and male mice were used for all mouse experiments to ensure that any sex-based variations in tumor development, progression, and response to intervention were captured. PDOs and TMAs were generated from both male and female CRC patients. Data were analyzed separately for male and female subjects first to discern any subtle sex-specific differences that may exist; however, no significant differences were observed between male and female subjects.

Generation of LIN28B^{high} cell lines

LoVo and DLD-1 cells were obtained from American Type Culture Collection (ATCC). LoVo and DLD-1 cells with LIN28B expression were generated using a previously described method (5, 12), as outlined in Supplemental Methods.

PDO culture

Tumor tissues were obtained from patients undergoing elective surgery at NewYork-Presbyterian/Columbia University Irving Medical Center with written informed consent under the protocol approved by the University of Columbia Institutional Review Board (IRB; protocol number AAAT8778). Organoid cultures were prepared as previously described, with minor modifications (78). To note, the protocol used for PDO establishment outlined in Supplemental Methods is also effective for tumor tissues that have been frozen in liquid nitrogen for up to 6 months.

Portal vein injection of LIN28B^{high} CRC cells

All animal studies were approved by the Institutional Animal Care and Use Committee (IACUC) at Columbia University, and all experiments were conducted in compliance with the National Institutes of Health (NIH) guidelines for animal research. Portal vein injection was performed as described previously (5) and is outlined in Supplemental Methods.

Generation of GEMMs

Villin^{Cre};Rosa26^{Pik3ca} mice were produced by mating B6.Cg-Tg(Vil1-cre)1000Gum/J mice (Jackson Laboratory, strain 021504) with C57BL/6-Gt(ROSA)26Sortm7(*Pik3ca**,EGFP)Rsky/J mice (Jackson Laboratory, strain 012343). *Villin^{CreERT};Rosa26^{Pik3ca}* mice resulted from crossing B6.Cg-Tg(Vil1-cre/ERT2)23Syr/J mice (Jackson Laboratory, strain 020282) with strain 012343. Both *Cre* and *CreERT* alleles were maintained in a hemizygous state. Toe clip samples were sent to TransnetYX for genotyping. Colon and SI were washed with cold PBS and collected as Swiss rolls before fixing in 10% neutral buffered formalin. In addition to genotyping, expression of mutant *Pik3ca* in the intestinal epithelial cells was confirmed by GFP expression, pAKT (Ser473) staining, and pAKT (Ser473) immunoblotting.

Western blot of cells and organoids

Immunoblotting was conducted as described in Supplemental Methods using primary antibodies (Supplemental Table 1) and visualized using IRDye secondary antibodies (LI-COR Biosciences 926-68070, 926-32211). Measured protein levels were normalized to either GAPDH or β-actin as endogenous controls.

PI3K/AKT pathway phosphorylation array

EV and LIN28B^{high} LoVo and DLD-1 cells, treated with either vehicle or alpelisib, were sent as frozen cell pellets to RayBiotech for analysis using the Human/Mouse AKT Pathway Phosphorylation Array (RayBiotech AAH-AKT-1).

Soft agar colony formation assay

The colony formation assay was performed using the CytoSelect 96-Well In Vitro Tumor Sensitivity Assay (Soft Agar Colony Formation, CBA-150) according to the manufacturer's instructions.

Construction of TMA

A cohort of 60 patients diagnosed with colon carcinoma was selected for the study. The patients' ages ranged from 44 to 94 years (mean age: 68.3 years). Rectal tumors were excluded from the study. The patients were selected based on the availability of primary tumors, normal adjacent colon tissue, and liver metastases. Tissue samples were obtained from patients, and TMAs were constructed by the Molecular Pathology Shared Resource under the University of Columbia IRB protocol AAAS3903. Three 2 mm cores of normal adjacent colon mucosa, primary tumor tissue, and liver metastases were collected from each patient and were paraffin-embedded in microarrays. IHC staining was performed on the TMA sections as described in Supplemental Methods.

Histopathologic analysis

All pathologic analyses were performed by Dr. Andres J. Klein-Szanto (Histopathology Facility, Fox Chase Cancer Center) in accordance with the consensus report and recommendations for pathologic analysis. The quantitative evaluation of positively stained cells (Ki-67, LIN28B, pAKT, pS6K, pRPS6) was performed by manually counting cells for each sample in a blinded fashion. For IHC analysis, 0 = negative staining involving < 33% of cells; 1 = weak staining involving 33 to 66% of cells; 2 = moderate staining involving >70% of cells; and 3 = strong staining involving >70% of cells.

Statistics

All data are presented as the mean ± standard error of the mean (SEM), and sample sizes are indicated in the graphs or figure legends. All studies were conducted with a minimum of three technical and biological replicates. Statistical significance was set at $P<0.05$. The statistical analyses, including Student's unpaired t-test, one-way ANOVA with Tukey's multiple comparisons test, two-way ANOVA with Tukey's or Sidak's multiple comparisons test, Chi-square tests, and Fisher's exact tests, were performed using GraphPad Prism version 10.4.0 for Windows (GraphPad Software, Boston, Massachusetts, USA; www.graphpad.com). *P<0.05, **P<0.01, ***P<0.001, ****P<0.0001. If the graphs do not display statistical annotations (asterisks) indicating significance, the results are not statistically significant (P>0.05). Statistical analyses were confirmed with The Cancer Biostatistics Shared Resource at Herbert Irving Comprehensive Cancer Center.

Study approval

All animal work and studies involving patient tissues were approved by the appropriate IRB approved by the University of Columbia. Written informed consent was obtained from all participants prior to their involvement in the study, in accordance with IRB guidelines.

Data availability

Values for all data points in graphs are reported in the Supporting Data Values file. RNA-seq data has been deposited in the GEO under the accession code GSE269369. Mouse models, 3D organoid lines, and engineered 2D cell lines are available from A.K.R. under a material transfer agreement with Columbia University.

Author contributions

AES and AKR conceptualized the study. Data curation and methodology were performed by AES and SPF. Formal analysis was conducted by AES, SPF, and AJK. Funding was acquired by AES, CJL, PAS, and AKR. Investigations were carried out by AES, KS, SWK, and NN. Project administration and supervision were managed by AES and AKR. Resources were provided by AES, DAC, JTG, and DD. Validation was performed by AES and SPF. Visualization was done by AES. The original draft was written by AES, SWK, and AKR. NV, CJL, PAS, and AKR contributed to review and editing.

Competing interests

Authors declare that they have no competing interests.

Acknowledgments

This study was supported by the Columbia University Digestive and Liver Disease Research Center (NIH grant 5P30DK132710) and the Herbert Irving Comprehensive Cancer Center (HICCC) (NIH grant P30CA013696) through use of the following shared resources: Confocal and Specialized Microscopy, Flow Cytometry (NIH grant S10OD020056), Molecular Pathology, Cancer Biostatistics, 3D Organoid and Cell Culture, and Genetically Modified Mouse Models.

Funding

NIH grant R01CA277795 (A.K.R.)

693 American Cancer Society grant PF-23-1149774-01-MM, https://doi.org/10.53354/ACS.PF-23-
694 1149774-01-MM.pc.gr.175458 (A.E.S.)
695 NIH grant P30CA013696 (A.K.R.)
696 NIH grant K08CA245192 (N.V.)
697 American Cancer Society grant PF-23-1151788-01-DMC, https://doi.org/10.53354/ACS.PF-23-
698 1151788-01-DMC.pc.gr.175436 (S.P.F.)
699 NIH grant 5P30DK132710 (A.K.R.)
700 NIH grant L30CA264714-01 (S.P.F.)

REFERENCES

1. Siegel RL, Giaquinto AN, and Jemal A. Cancer statistics, 2024. *CA Cancer J Clin.* 2024;74(1):12-49.
2. American Cancer Society. Survival Rates for Colorectal Cancer. https://www.cancer.org/cancer/types/colon-rectal-cancer/detection-diagnosis-staging/survival-rates.html. Updated January 29, 2024. Accessed September 1, 2024.
3. Vogelstein B, Fearon ER, Hamilton SR, Kern SE, Preisinger AC, Leppert M, et al. Genetic alterations during colorectal-tumor development. *N Engl J Med.* 1988;319(9):525-32.
4. Madison BB, Liu Q, Zhong X, Hahn CM, Lin N, Emmett MJ, et al. LIN28B promotes growth and tumorigenesis of the intestinal epithelium via Let-7. *Genes Dev.* 2013;27(20):2233-45.
5. Sugiura K, Masuike Y, Suzuki K, Shin AE, Sakai N, Matsubara H, et al. LIN28B promotes cell invasion and colorectal cancer metastasis via CLDN1 and NOTCH3. *JCI Insight.* 2023;8(14).
6. Polesskaya A, Cuvellier S, Naguibneva I, Duquet A, Moss EG, and Harel-Bellan A. Lin-28 binds IGF-2 mRNA and participates in skeletal myogenesis by increasing translation efficiency. *Genes Dev.* 2007;21(9):1125-38.
7. Xu B, and Huang Y. Histone H2a mRNA interacts with Lin28 and contains a Lin28-dependent posttranscriptional regulatory element. *Nucleic Acids Res.* 2009;37(13):4256-63.

8. Qiu C, Ma Y, Wang J, Peng S, and Huang Y. Lin28-mediated post-transcriptional regulation of Oct4 expression in human embryonic stem cells. *Nucleic Acids Res.* 2010;38(4):1240-8.

9. Wilbert ML, Huelga SC, Kapeli K, Stark TJ, Liang TY, Chen SX, et al. LIN28 binds messenger RNAs at GGAGA motifs and regulates splicing factor abundance. *Mol Cell.* 2012;48(2):195-206.

10. Hafner M, Max KE, Bandaru P, Morozov P, Gerstberger S, Brown M, et al. Identification of mRNAs bound and regulated by human LIN28 proteins and molecular requirements for RNA recognition. *RNA.* 2013;19(5):613-26.

11. Tu HC, Schwitalla S, Qian Z, LaPier GS, Yermalovich A, Ku YC, et al. LIN28 cooperates with WNT signaling to drive invasive intestinal and colorectal adenocarcinoma in mice and humans. *Genes Dev.* 2015;29(10):1074-86.

12. King CE, Cuatrecasas M, Castells A, Sepulveda AR, Lee JS, and Rustgi AK. LIN28B promotes colon cancer progression and metastasis. *Cancer Res.* 2011;71(12):4260-8.

13. Hamano R, Miyata H, Yamasaki M, Sugimura K, Tanaka K, Kurokawa Y, et al. High expression of Lin28 is associated with tumour aggressiveness and poor prognosis of patients in oesophagus cancer. *Br J Cancer.* 2012;106(8):1415-23.

14. Suzuki K, Masuike Y, Mizuno R, Sachdeva UM, Chatterji P, Andres SF, et al. LIN28B induces a differentiation program through CDX2 in colon cancer. *JCI Insight.* 2021;6(9).

15. Fruman DA, Chiu H, Hopkins BD, Bagrodia S, Cantley LC, and Abraham RT. The PI3K Pathway in Human Disease. *Cell.* 2017;170(4):605-35.

16. Vanhaesebroeck B, Vogt PK, and Rommel C. PI3K: from the bench to the clinic and back. *Curr Top Microbiol Immunol.* 2010;347:1-19.

17. Weng QP, Andrabi K, Klippel A, Kozlowski MT, Williams LT, and Avruch J. Phosphatidylinositol 3-kinase signals activation of p70 S6 kinase in situ through site-specific p70 phosphorylation. *Proc Natl Acad Sci U S A.* 1995;92(12):5744-8.

18. Burgering BM, and Coffer PJ. Protein kinase B (c-Akt) in phosphatidylinositol-3-OH kinase signal transduction. *Nature.* 1995;376(6541):599-602.

19. Vanhaesebroeck B, Perry MWD, Brown JR, Andre F, and Okkenhaug K. PI3K inhibitors are finally coming of age. *Nat Rev Drug Discov.* 2021;20(10):741-69.

20. Markowitz SD, and Bertagnolli MM. Molecular origins of cancer: Molecular basis of colorectal cancer. *N Engl J Med.* 2009;361(25):2449-60.

21. Okkenhaug K, Graupera M, and Vanhaesebroeck B. Targeting PI3K in Cancer: Impact on Tumor Cells, Their Protective Stroma, Angiogenesis, and Immunotherapy. *Cancer Discov.* 2016;6(10):1090-105.

22. Liang S, Guo H, Ma K, Li X, Wu D, Wang Y, et al. A PLCB1-PI3K-AKT Signaling Axis Activates EMT to Promote Cholangiocarcinoma Progression. *Cancer Res.* 2021;81(23):5889-903.

23. Maharati A, and Moghbeli M. PI3K/AKT signaling pathway as a critical regulator of epithelial-mesenchymal transition in colorectal tumor cells. *Cell Commun Signal.* 2023;21(1):201.

24. Yaeger R, Chatila WK, Lipsyc MD, Hechtman JF, Cercek A, Sanchez-Vega F, et al. Clinical Sequencing Defines the Genomic Landscape of Metastatic Colorectal Cancer. *Cancer Cell.* 2018;33(1):125-36 e3.

25. Priestley P, Baber J, Lolkema MP, Steeghs N, de Bruijn E, Shale C, et al. Pan-cancer whole-genome analyses of metastatic solid tumours. *Nature.* 2019;575(7781):210-6.

26. Mendelaar PAJ, Smid M, van Riet J, Angus L, Labots M, Steeghs N, et al. Whole genome sequencing of metastatic colorectal cancer reveals prior treatment effects and specific metastasis features. *Nat Commun.* 2021;12(1):574.

27. Sartore-Bianchi A, Martini M, Molinari F, Veronese S, Nichelatti M, Artale S, et al. PIK3CA mutations in colorectal cancer are associated with clinical resistance to EGFR-targeted monoclonal antibodies. *Cancer Res.* 2009;69(5):1851-7.

28. Gowrikumar S, Primeaux M, Pravoverov K, Wu C, Szeglin BC, Sauve CG, et al. A Claudin-Based Molecular Signature Identifies High-Risk, Chemoresistant Colorectal Cancer Patients. *Cells.* 2021;10(9).

29. Malinowsky K, Nitsche U, Janssen KP, Bader FG, Spath C, Drecoll E, et al. Activation of the PI3K/AKT pathway correlates with prognosis in stage II colon cancer. *Br J Cancer.* 2014;110(8):2081-9.

30. Wang L, Hu H, Pan Y, Wang R, Li Y, Shen L, et al. PIK3CA mutations frequently coexist with EGFR/KRAS mutations in non-small cell lung cancer and suggest poor prognosis in EGFR/KRAS wildtype subgroup. *PLoS One.* 2014;9(2):e88291.

31. Jhaveri K, Chang MT, Juric D, Saura C, Gambardella V, Melnyk A, et al. Phase I Basket Study of Taselisib, an Isoform-Selective PI3K Inhibitor, in Patients with PIK3CA-Mutant Cancers. *Clin Cancer Res.* 2021;27(2):447-59.

32. Juric D, Rodon J, Tabernero J, Janku F, Burris HA, Schellens JHM, et al. Phosphatidylinositol 3-Kinase alpha-Selective Inhibition With Alpelisib (BYL719) in PIK3CA-Altered Solid Tumors: Results From the First-in-Human Study. *J Clin Oncol.* 2018;36(13):1291-9.

33. Gouda MA, and Subbiah V. Precision oncology for BRAF-mutant cancers with BRAF and MEK inhibitors: from melanoma to tissue-agnostic therapy. *ESMO Open.* 2023;8(2):100788.

34. Varkaris A, Pazolli E, Gunaydin H, Wang Q, Pierce L, Boezio AA, et al. Discovery and clinical proof-of-concept of RLY-2608, a first-in-class mutant-selective allosteric PI3Ka inhibitor that decouples anti-tumor activity from hyperinsulinemia. *Cancer Discov.* 2023.

35. Buckbinder L, St Jean DJ, Jr., Tieu T, Ladd B, Hilbert B, Wang W, et al. STX-478, a Mutant-Selective, Allosteric PI3Kalpha Inhibitor Spares Metabolic Dysfunction and Improves Therapeutic Response in PI3Kalpha-Mutant Xenografts. *Cancer Discov.* 2023;13(11):2432-47.

36. Shin AE, Giancotti FG, and Rustgi AK. Metastatic colorectal cancer: mechanisms and emerging therapeutics. *Trends Pharmacol Sci.* 2023;44(4):222-36.

37. Madison BB, Dunbar L, Qiao XT, Braunstein K, Braunstein E, and Gumucio DL. Cis elements of the villin gene control expression in restricted domains of the vertical (crypt) and horizontal (duodenum, cecum) axes of the intestine. *J Biol Chem.* 2002;277(36):33275-83.

38. Srinivasan L, Sasaki Y, Calado DP, Zhang B, Paik JH, DePinho RA, et al. PI3 kinase signals BCR-dependent mature B cell survival. *Cell.* 2009;139(3):573-86.

39. Hoxhaj G, and Manning BD. The PI3K-AKT network at the interface of oncogenic signalling and cancer metabolism. *Nat Rev Cancer.* 2020;20(2):74-88.

40. Moskaluk CA, Zhang H, Powell SM, Cerilli LA, Hampton GM, and Frierson HF, Jr. Cdx2 protein expression in normal and malignant human tissues: an immunohistochemical survey using tissue microarrays. *Mod Pathol.* 2003;16(9):913-9.

41. el Marjou F, Janssen KP, Chang BH, Li M, Hindie V, Chan L, et al. Tissue-specific and inducible Cre-mediated recombination in the gut epithelium. *Genesis.* 2004;39(3):186-93.

42. Guda K, Cui H, Garg S, Dong M, Nambiar PR, Achenie LE, et al. Multistage gene expression profiling in a differentially susceptible mouse colon cancer model. *Cancer Lett.* 2003;191(1):17-25.

43. Li C, Lau HC, Zhang X, and Yu J. Mouse Models for Application in Colorectal Cancer: Understanding the Pathogenesis and Relevance to the Human Condition. *Biomedicines.* 2022;10(7).

44. Shin AE, Tesfagiorgis Y, Larsen F, Derouet M, Zeng PYF, Good HJ, et al. F4/80+Ly6Chigh Macrophages Lead to Cell Plasticity and Cancer Initiation in Colitis. *Gastroenterology.* 2023;164(4):593-609.e13.

45. Andre F, Ciruelos E, Rubovszky G, Campone M, Loibl S, Rugo HS, et al. Alpelisib for PIK3CA-Mutated, Hormone Receptor-Positive Advanced Breast Cancer. *N Engl J Med.* 2019;380(20):1929-40.

46. Razavi P, Dickler MN, Shah PD, Toy W, Brown DN, Won HH, et al. Alterations in PTEN and ESR1 promote clinical resistance to alpelisib plus aromatase inhibitors. *Nat Cancer.* 2020;1(4):382-93.

47. Kim SK, Kim SY, Kim JH, Roh SA, Cho DH, Kim YS, et al. A nineteen gene-based risk score classifier predicts prognosis of colorectal cancer patients. *Mol Oncol.* 2014;8(8):1653-66.

48. Manning BD, and Toker A. AKT/PKB Signaling: Navigating the Network. *Cell.* 2017;169(3):381-405.

49. Saxton RA, and Sabatini DM. mTOR Signaling in Growth, Metabolism, and Disease. *Cell.* 2017;169(2):361-71.

50. Turner NC, Oliveira M, Howell SJ, Dalenc F, Cortes J, Gomez Moreno HL, et al. Capivasertib in Hormone Receptor-Positive Advanced Breast Cancer. *N Engl J Med.* 2023;388(22):2058-70.

51. Taketo MM, and Edelmann W. Mouse models of colon cancer. *Gastroenterology.* 2009;136(3):780-98.

52. Hung KE, Maricevich MA, Richard LG, Chen WY, Richardson MP, Kunin A, et al. Development of a mouse model for sporadic and metastatic colon tumors and its use in assessing drug treatment. *Proc Natl Acad Sci U S A.* 2010;107(4):1565-70.

53. Boutin AT, Liao WT, Wang M, Hwang SS, Karpinets TV, Cheung H, et al. Oncogenic Kras drives invasion and maintains metastases in colorectal cancer. *Genes Dev.* 2017;31(4):370-82.

54. Varga J, Nicolas A, Petrocelli V, Pesic M, Mahmoud A, Michels BE, et al. AKT-dependent NOTCH3 activation drives tumor progression in a model of mesenchymal colorectal cancer. *J Exp Med.* 2020;217(10).

55. Schwitalla S, Ziegler PK, Horst D, Becker V, Kerle I, Begus-Nahrmann Y, et al. Loss of p53 in enterocytes generates an inflammatory microenvironment enabling invasion and lymph node metastasis of carcinogen-induced colorectal tumors. *Cancer Cell.* 2013;23(1):93-106.

56. O'Rourke KP, Loizou E, Livshits G, Schatoff EM, Baslan T, Manchado E, et al. Transplantation of engineered organoids enables rapid generation of metastatic mouse models of colorectal cancer. *Nat Biotechnol.* 2017;35(6):577-82.

57. de Sousa e Melo F, Kurtova AV, Harnoss JM, Kljavin N, Hoeck JD, Hung J, et al. A distinct role for Lgr5(+) stem cells in primary and metastatic colon cancer. *Nature.* 2017;543(7647):676-80.

58. Yuan W, Stawiski E, Janakiraman V, Chan E, Durinck S, Edgar KA, et al. Conditional activation of Pik3ca(H1047R) in a knock-in mouse model promotes mammary tumorigenesis and emergence of mutations. *Oncogene.* 2013;32(3):318-26.

59. Vasan N, and Cantley LC. At a crossroads: how to translate the roles of PI3K in oncogenic and metabolic signalling into improvements in cancer therapy. *Nat Rev Clin Oncol.* 2022;19(7):471-85.

60. Mitchell CB, and Phillips WA. Mouse Models for Exploring the Biological Consequences and Clinical Significance of PIK3CA Mutations. *Biomolecules.* 2019;9(4).

61. Koren S, and Bentires-Alj M. Mouse models of PIK3CA mutations: one mutation initiates heterogeneous mammary tumors. *FEBS J.* 2013;280(12):2758-65.

62. Vlachogiannis G, Hedayat S, Vatsiou A, Jamin Y, Fernandez-Mateos J, Khan K, et al. Patient-derived organoids model treatment response of metastatic gastrointestinal cancers. *Science.* 2018;359(6378):920-6.

63. Liu J, Cho YB, Hong HK, Wu S, Ebert PJ, Bray SM, et al. Molecular dissection of CRC primary tumors and their matched liver metastases reveals critical role of immune microenvironment, EMT and angiogenesis in cancer metastasis. *Sci Rep.* 2020;10(1):10725.

64. Lee SE, Park HY, Hwang DY, and Han HS. High Concordance of Genomic Profiles between Primary and Metastatic Colorectal Cancer. *Int J Mol Sci.* 2021;22(11).

65. Ham-Karim H, Negm O, Ahmad N, and Ilyas M. Investigating genomic, proteomic, and post-transcriptional regulation profiles in colorectal cancer: a comparative study between primary tumors and associated metastases. *Cancer Cell Int.* 2023;23(1):192.

66. Kamal Y, Schmit SL, Hoehn HJ, Amos CI, and Frost HR. Transcriptomic Differences between Primary Colorectal Adenocarcinomas and Distant Metastases Reveal Metastatic Colorectal Cancer Subtypes. *Cancer Res.* 2019;79(16):4227-41.

67. Gray J. Cancer: Genomics of metastasis. *Nature.* 2010;464(7291):989-90.

68. Janku F, Lee JJ, Tsimberidou AM, Hong DS, Naing A, Falchook GS, et al. PIK3CA mutations frequently coexist with RAS and BRAF mutations in patients with advanced cancers. *PLoS One.* 2011;6(7):e22769.

69. Voutsina A, Tzardi M, Kalikaki A, Zafeiriou Z, Papadimitraki E, Papadakis M, et al. Combined analysis of KRAS and PIK3CA mutations, MET and PTEN expression in primary tumors and corresponding metastases in colorectal cancer. *Mod Pathol.* 2013;26(2):302-13.

70. Luo Q, Chen D, Fan X, Fu X, Ma T, and Chen D. KRAS and PIK3CA bi-mutations predict a poor prognosis in colorectal cancer patients: A single-site report. *Transl Oncol.* 2020;13(12):100874.

71. Serebriiskii IG, Connelly C, Frampton G, Newberg J, Cooke M, Miller V, et al. Comprehensive characterization of RAS mutations in colon and rectal cancers in old and young patients. *Nat Commun.* 2019;10(1):3722.

72. Turner NC, Im SA, Saura C, Juric D, Loibl S, Kalinsky K, et al. Inavolisib-Based Therapy in PIK3CA-Mutated Advanced Breast Cancer. *N Engl J Med.* 2024;391(17):1584-96.

73. Hollebecque A, Houede N, Cohen EE, Massard C, Italiano A, Westwood P, et al. A phase Ib trial of LY2584702 tosylate, a p70 S6 inhibitor, in combination with erlotinib or everolimus in patients with solid tumours. *Eur J Cancer.* 2014;50(5):876-84.

74. Tolcher A, Goldman J, Patnaik A, Papadopoulos KP, Westwood P, Kelly CS, et al. A phase I trial of LY2584702 tosylate, a p70 S6 kinase inhibitor, in patients with advanced solid tumours. *Eur J Cancer.* 2014;50(5):867-75.

75. Larkin J, Ascierto PA, Dreno B, Atkinson V, Liszkay G, Maio M, et al. Combined vemurafenib and cobimetinib in BRAF-mutated melanoma. *N Engl J Med.* 2014;371(20):1867-76.

76. Davies MA, Saiag P, Robert C, Grob JJ, Flaherty KT, Arance A, et al. Dabrafenib plus trametinib in patients with BRAF(V600)-mutant melanoma brain metastases (COMBI-MB): a multicentre, multicohort, open-label, phase 2 trial. *Lancet Oncol.* 2017;18(7):863-73.

77. Long GV, Hauschild A, Santinami M, Atkinson V, Mandala M, Chiarion-Sileni V, et al. Adjuvant Dabrafenib plus Trametinib in Stage III BRAF-Mutated Melanoma. *N Engl J Med.* 2017;377(19):1813-23.

78. Sato T, Stange DE, Ferrante M, Vries RG, Van Es JH, Van den Brink S, et al. Long-term expansion of epithelial organoids from human colon, adenoma, adenocarcinoma, and Barrett's epithelium. *Gastroenterology.* 2011;141(5):1762-72.

FIGURES AND FIGURE LEGENDS

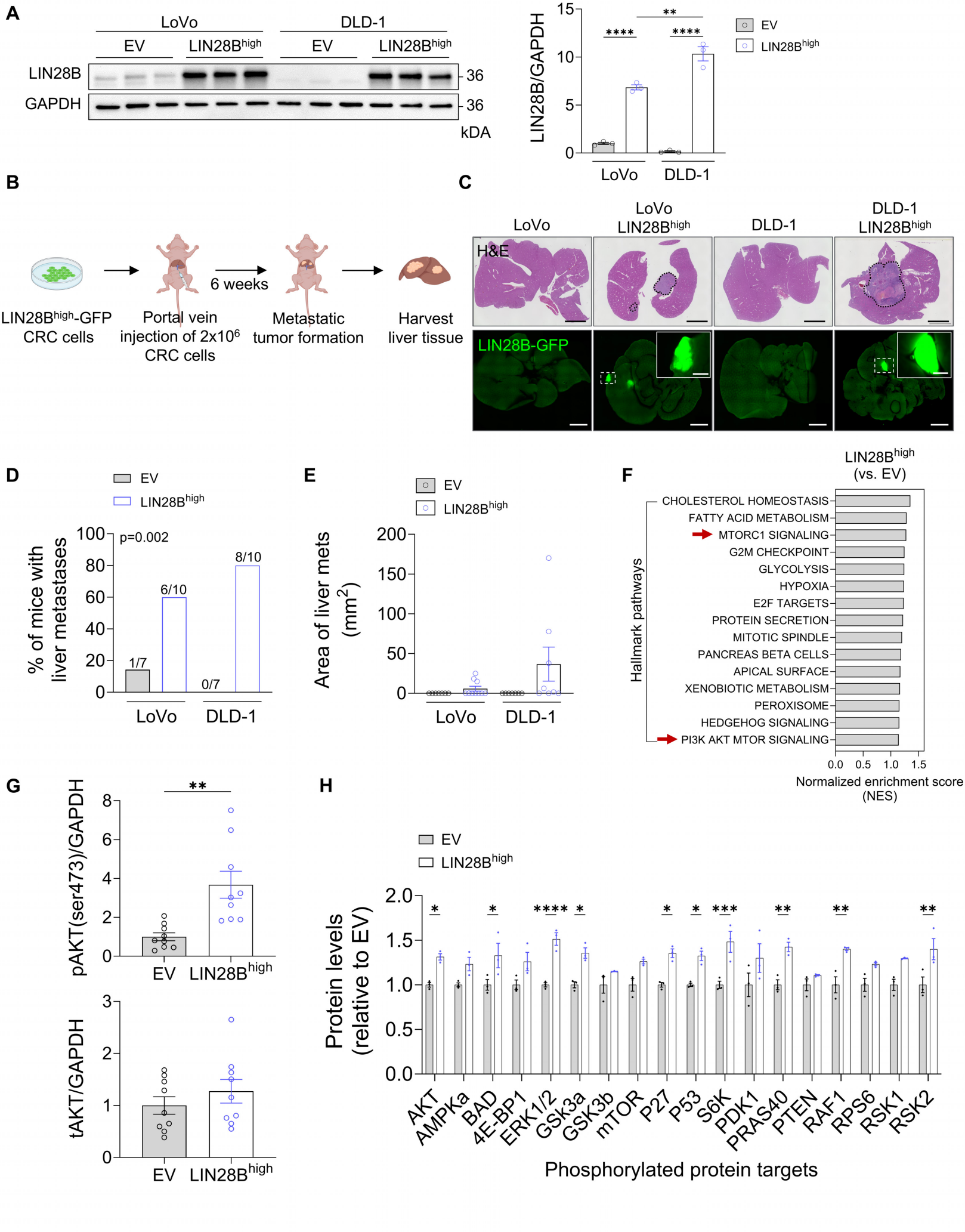
A
LoVo
DLD-1
EV
LIN28B^high
LIN28B
GAPDH
36
36
kDA
LIN28B/GAPDH
15
10
5
0
**
****
****
EV
LIN28B^high
LoVo
DLD-1
B
LIN28B^high-GFP CRC cells
Portal vein injection of 2x10^6 CRC cells
6 weeks
Metastatic tumor formation
Harvest liver tissue
C
LoVo
LoVo LIN28B^high
DLD-1
DLD-1 LIN28B^high
H&E
LIN28B-GFP
D
EV
LIN28B^high
% of mice with liver metastases
100
80
60
40
20
0
p=0.002
1/7
6/10
0/7
8/10
LoVo
DLD-1
E
EV
LIN28B^high
Area of liver mets (mm^2)
200
150
100
50
0
LoVo
DLD-1
F
LIN28B^high (vs. EV)
Hallmark pathways
CHOLESTEROL HOMEOSTASIS
FATTY ACID METABOLISM
MTORC1 SIGNALING
G2M CHECKPOINT
GLYCOLYSIS
HYPOXIA
E2F TARGETS
PROTEIN SECRETION
MITOTIC SPINDLE
PANCREAS BETA CELLS
APICAL SURFACE
XENOBIOTIC METABOLISM
PEROXISOME
HEDGEHOG SIGNALING
PI3K AKT MTOR SIGNALING
0.0
0.5
1.0
1.5
Normalized enrichment score (NES)
G
pAKT(ser473)/GAPDH
8
6
4
2
0
**
EV
LIN28B^high
tAKT/GAPDH
3
2
1
0
EV
LIN28B^high
H
EV
LIN28B^high
Protein levels (relative to EV)
2.0
1.5
1.0
0.5
0.0
AKT
AMPKa
BAD
4E-BP1
ERK1/2
GSk3a
GSK3b
mTOR
P27
P53
S6K
PDK1
PRAS40
PTEN
RAF1
RPS6
RSK1
RSK2
Phosphorylated protein targets

Figure 1: LIN28B expression in CRC cells activates the PI3K/AKT pathway and promotes liver metastasis. **(A)** Western blot of LIN28B protein levels in LoVo and DLD-1 CRC cell lines with either EV or LIN28B overexpression vector (LIN28B^{high}), normalized to GAPDH and LoVo EV (one-way ANOVA, mean ± SEM). **(B)** Experimental setup for in vivo colorectal liver metastasis assay. **(C)** Representative H&E and GFP images of liver sections from mice injected with CRC cells. Scale bars = 5 mm, scale bars for insets = 1 mm. **(D)** Proportion of mice that developed liver metastases (Chi-square test). **(E)** Quantification of the size of liver metastases in each group (one-way ANOVA, mean ± SEM). **(F)** GSEA showing hallmark pathways enriched in LoVo LIN28B^{high} cells compared to EV cells (n=3). **(G)** Western blot analysis of pAKT (Ser473) and tAKT in CRC cells (Student's unpaired t-test, mean ± SEM). **(H)** Quantification of phosphorylated protein targets involved in the PI3K/AKT pathway in LIN28B^{high} cells relative to EV cells as measured by AKT Pathway Phosphorylation Array (Student's unpaired t-test between EV and LIN28B^{high} for each protein, mean ± SEM).

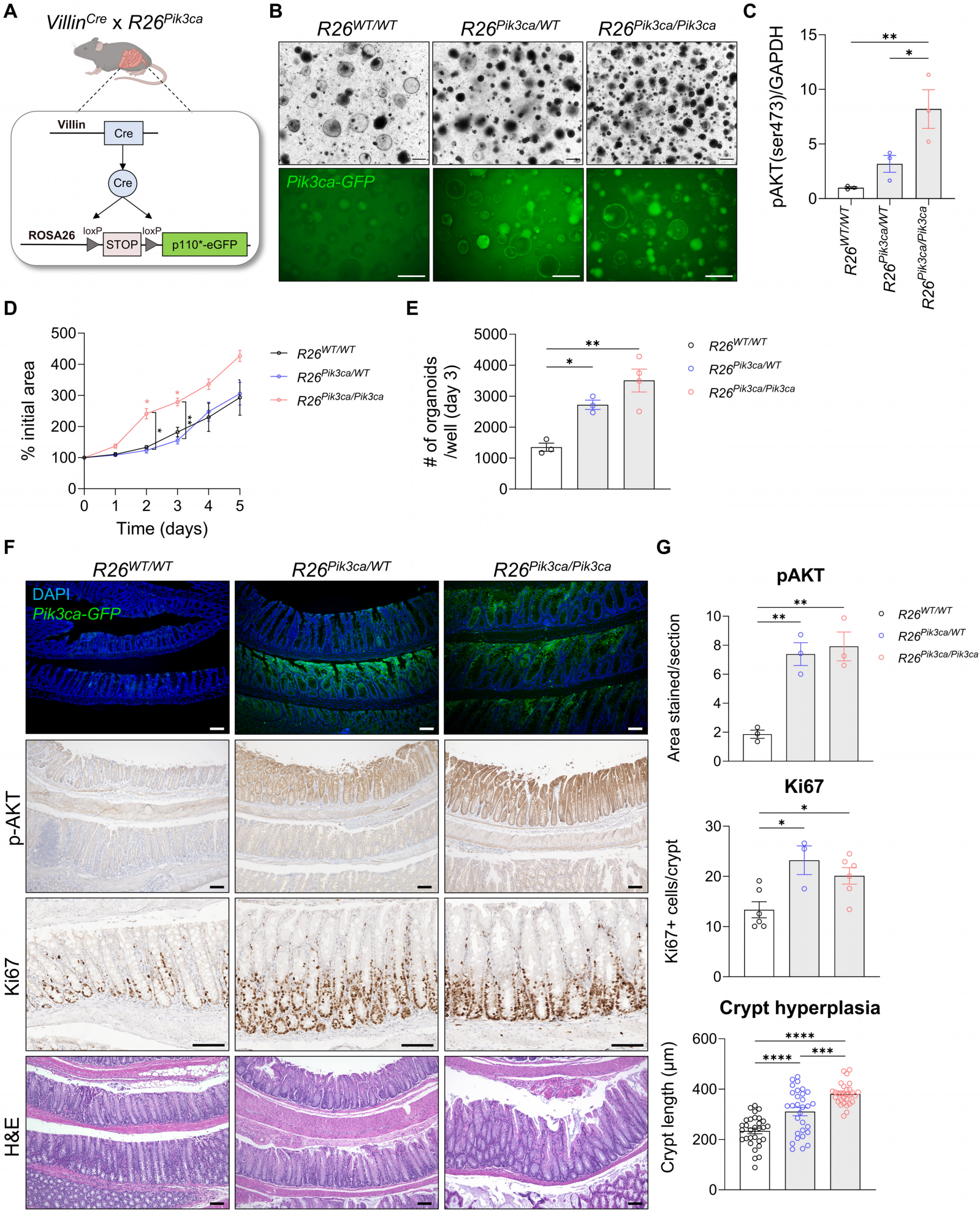
A
Villin^Cre x R26^Pik3ca
Villin
Cre
Cre
ROSA26
loxP
STOP
loxP
p110*-eGFP
B
R26^WT/WT
R26^Pik3ca/WT
R26^Pik3ca/Pik3ca
Pik3ca-GFP
C
pAKT(ser473)/GAPDH
R26^WT/WT
R26^Pik3ca/WT
R26^Pik3ca/Pik3ca
D
% initial area
Time (days)
R26^WT/WT
R26^Pik3ca/WT
R26^Pik3ca/Pik3ca
E
# of organoids /well (day 3)
R26^WT/WT
R26^Pik3ca/WT
R26^Pik3ca/Pik3ca
F
R26^WT/WT
R26^Pik3ca/WT
R26^Pik3ca/Pik3ca
DAPI
Pik3ca-GFP
p-AKT
Ki67
H&E
G
pAKT
Area stained/section
Ki67
Ki67+ cells/crypt
Crypt hyperplasia
Crypt length (μm)
R26^WT/WT
R26^Pik3ca/WT
R26^Pik3ca/Pik3ca

Figure 2: Genetic activation of the PI3K/AKT pathway enhances organoid growth ex vivo and induces colonic crypt hyperplasia in vivo. (A) Schematic representation of the genetic cross to generate *Villin*^{Cre}*;R26*^{Pik3ca} mice on a C57BL/6J background. **(B)** Representative brightfield and GFP images of colonic organoids derived from *R26*$^{WT/WT}$, *R26*$^{Pik3ca/WT}$, and *R26*$^{Pik3ca/Pik3ca}$ mice cultured for 5 days. Scale bars = 500 μm (n=3). **(C)** Immunoblot quantification of pAKT (Ser473) levels relative to GAPDH in colonic organoids derived from *R26*$^{WT/WT}$, *R26*$^{Pik3ca/WT}$, and *R26*$^{Pik3ca/Pik3ca}$ mice, normalized to *R26*$^{WT/WT}$ (n=3; one-way ANOVA, mean ± SEM). **(D)** Quantification of growth of colonic organoids from *R26*$^{WT/WT}$, *R26*$^{Pik3ca/WT}$, and *R26*$^{Pik3ca/Pik3ca}$ mice, showing percent increase in initial area (n=3 and 4, two-way ANOVA, mean ± SEM). **(E)** Quantification of the number of colonic organoids per well on day 3 of culture (one-way ANOVA, mean ± SEM). **(F)** Representative immunofluorescence and IHC images of colonic tissues from *R26*$^{WT/WT}$, *R26*$^{Pik3ca/WT}$, and *R26*$^{Pik3ca/Pik3ca}$ mice, showing *Pik3ca*-GFP, pAKT (Ser473), Ki67, and H&E staining. Scale bars = 100 μm. **(G)** Quantification of pAKT-stained area per section, Ki67+ cells per crypt, and crypt length in colonic tissues from *R26*$^{WT/WT}$, *R26*$^{Pik3ca/WT}$, and *R26*$^{Pik3ca/Pik3ca}$ mice. Crypt length was measured every 100 μm along the length of the colon (one-way ANOVA, mean ± SEM).

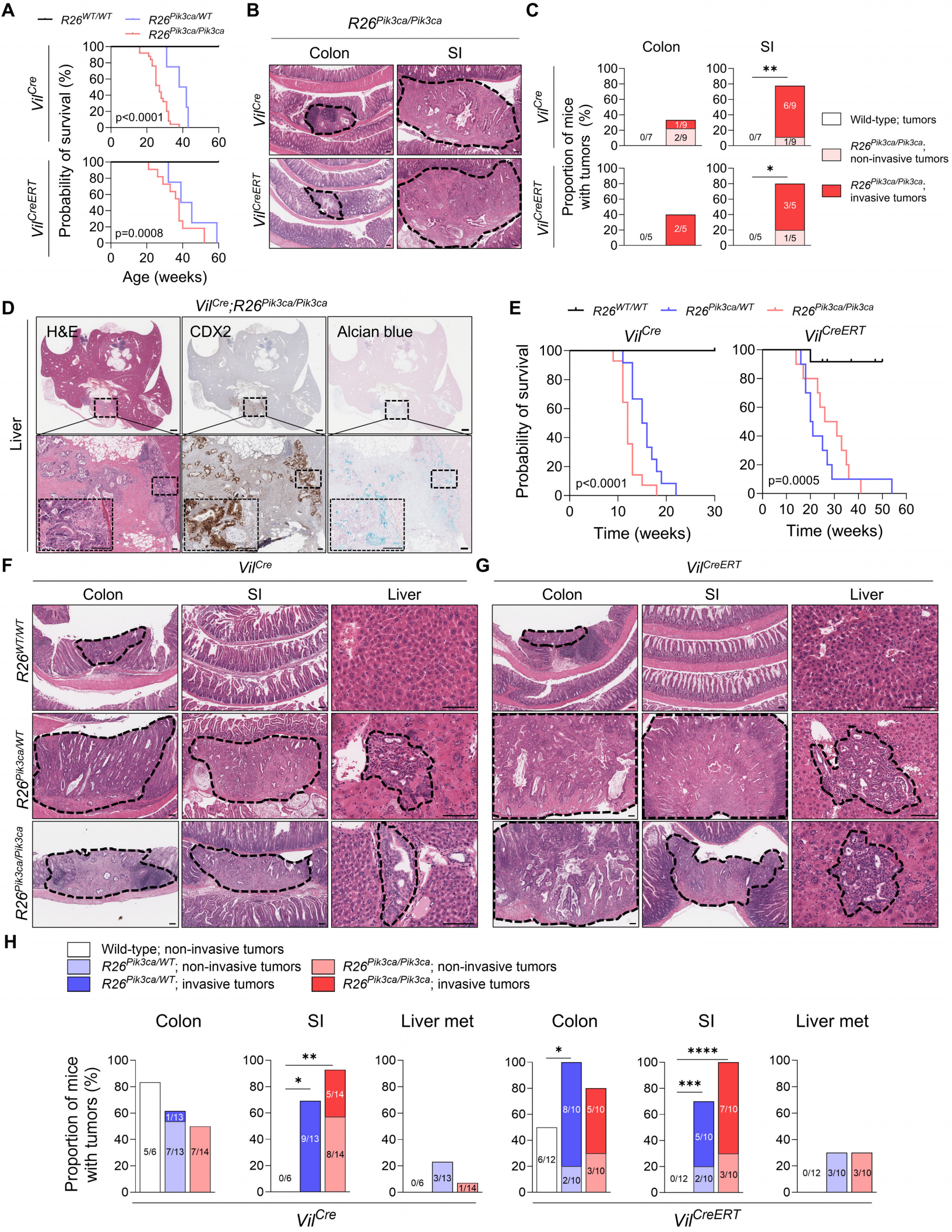
A
R26WT/WT
R26Pik3ca/WT
R26Pik3ca/Pik3ca
VilCre
VilCreERT
Probability of survival (%)
p<0.0001
p=0.0008
Age (weeks)
B
R26Pik3ca/Pik3ca
Colon
SI
VilCre
VilCreERT
C
Colon
SI
Proportion of mice with tumors (%)
0/7
1/9
2/9
0/7
6/9
1/9
0/5
2/5
0/5
3/5
1/5
Wild-type; tumors
R26Pik3ca/Pik3ca; non-invasive tumors
R26Pik3ca/Pik3ca; invasive tumors
D
VilCre;R26Pik3ca/Pik3ca
Liver
H&E
CDX2
Alcian blue
E
R26WT/WT
R26Pik3ca/WT
R26Pik3ca/Pik3ca
VilCre
VilCreERT
Probability of survival
p<0.0001
p=0.0005
Time (weeks)
F
VilCre
Colon
SI
Liver
R26WT/WT
R26Pik3ca/WT
R26Pik3ca/Pik3ca
G
VilCreERT
Colon
SI
Liver
H
Wild-type; non-invasive tumors
R26Pik3ca/WT; non-invasive tumors
R26Pik3ca/WT; invasive tumors
R26Pik3ca/Pik3ca; non-invasive tumors
R26Pik3ca/Pik3ca; invasive tumors
Colon
SI
Liver met
Proportion of mice with tumors (%)
5/6
1/13
7/13
7/14
0/6
9/13
5/14
8/14
0/6
3/13
1/14
6/12
8/10
2/10
5/10
3/10
0/12
5/10
2/10
7/10
3/10
0/12
3/10
3/10
VilCre
VilCreERT

Figure 3: Genetic activation of the PI3K/AKT pathway promotes tumorigenesis, tumor invasiveness, and liver metastasis in a mouse model of CRC. (A) Kaplan-Meier survival curves of *Villin*^{Cre} and *Villin*^{CreERT2} mice with either *R26*$^{WT/WT}$, *R26*$^{Pik3ca/WT}$, or *R26*$^{Pik3ca/Pik3ca}$ genotype (n=7, 4, and 25 for *Villin*^{Cre}, n=5, 4, and 11 for *Villin*^{CreERT}; log-rank test). **(B)** Representative H&E images of the colon and SI tissues from mice with *R26*$^{Pik3ca/Pik3ca}$ genotype. Dotted lines outline the tumors. Scale bars = 100 μm. **(C)** Proportion of mice with non-invasive adenomas and invasive adenocarcinomas in the colon and SI from *Villin*^{Cre} and *Villin*^{CreERT2} mice with either *R26*$^{WT/WT}$ or *R26*$^{Pik3ca/Pik3ca}$ genotype (Fisher's exact test). **(D)**. Representative H&E, CDX2, and Alcian blue staining of a liver metastasis from a 28-weeks old *Vil*^{Cre}*;R26*$^{Pik3ca/Pik3ca}$ mouse. Scale bars = 1 mm, scale bars for insets = 100 μm. **(E)** Kaplan-Meier survival curves of *Villin*^{Cre} and *Villin*^{CreERT2} mice treated with AOM and tamoxifen (n=8-14 *Villin*^{Cre}, n=10-12 for *Villin*^{CreERT}; log-rank test). **(F** and **G)** Representative H&E images of the colon, SI, and liver tissues from *Vil*^{Cre} (F) and *Villin*^{CreERT2} (G) mice treated with AOM. Dotted lines outline the tumors. Scale bars = 100 μm **(H)** Proportion of mice with non-invasive adenomas and invasive adenocarcinomas in the colon and SI, and liver metastases from mice treated with AOM (Chi-square test between *R26*$^{WT/WT}$ and either *R26*$^{Pik3ca/WT}$ or *R26*$^{Pik3ca/Pik3ca}$ genotype).

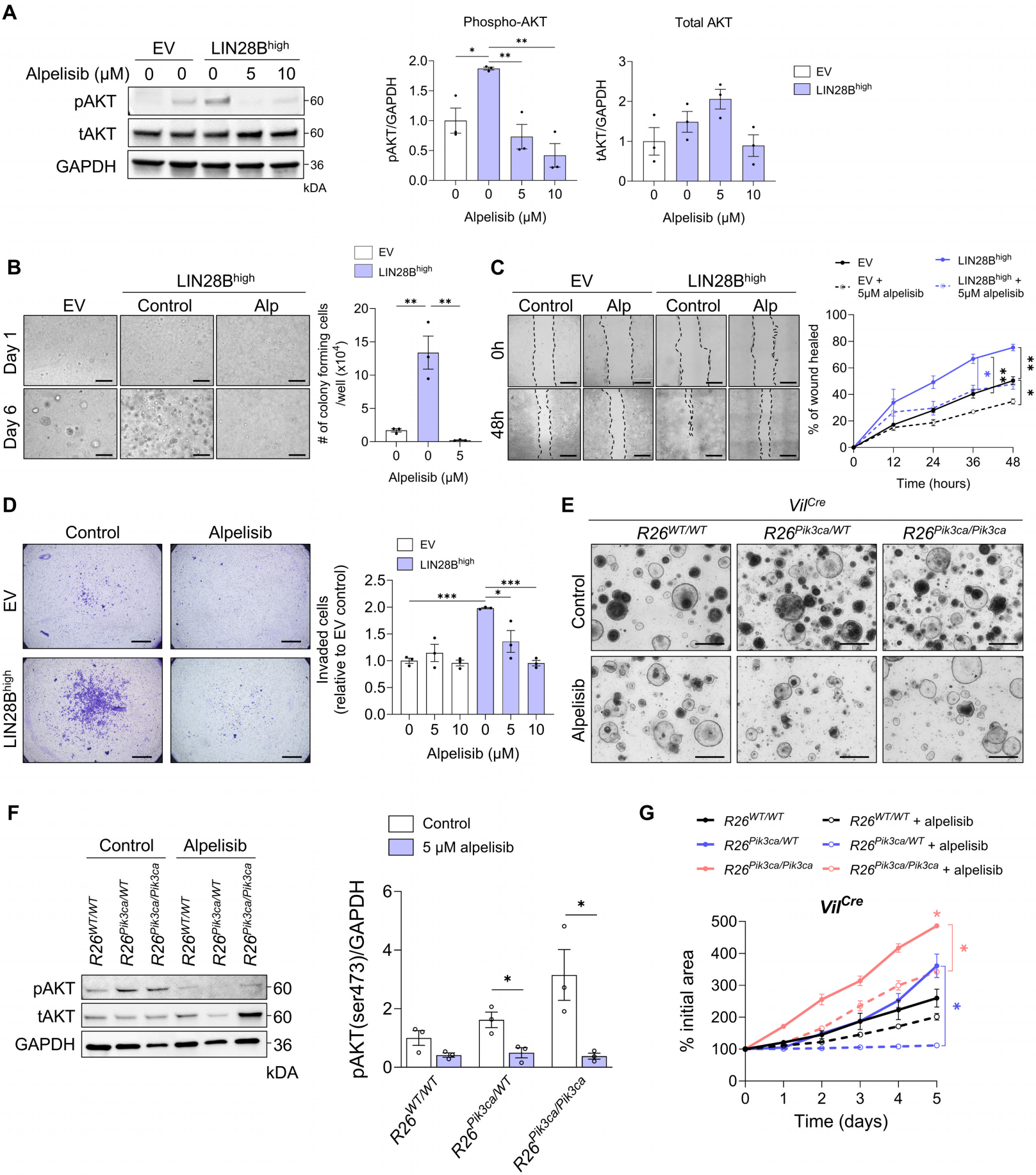
A
EV
LIN28B^high
Alpelisib (μM) 0 0 0 5 10
pAKT
tAKT
GAPDH
60
60
36
kDA
Phospho-AKT
pAKT/GAPDH
Alpelisib (μM)
Total AKT
tAKT/GAPDH
Alpelisib (μM)
EV
LIN28B^high
B
LIN28B^high
EV
Control
Alp
Day 1
Day 6
# of colony forming cells /well (x10^4)
Alpelisib (μM)
C
EV
LIN28B^high
Control
Alp
0h
48h
EV
EV + 5μM alpelisib
LIN28B^high
LIN28B^high + 5μM alpelisib
% of wound healed
Time (hours)
D
Control
Alpelisib
EV
LIN28B^high
Invaded cells (relative to EV control)
Alpelisib (μM)
E
Vil^Cre
R26^WT/WT
R26^Pik3ca/WT
R26^Pik3ca/Pik3ca
Control
Alpelisib
F
Control
Alpelisib
R26^WT/WT
R26^Pik3ca/WT
R26^Pik3ca/Pik3ca
pAKT
tAKT
GAPDH
60
60
36
kDA
Control
5 μM alpelisib
pAKT(ser473)/GAPDH
G
R26^WT/WT
R26^WT/WT + alpelisib
R26^Pik3ca/WT
R26^Pik3ca/WT + alpelisib
R26^Pik3ca/Pik3ca
R26^Pik3ca/Pik3ca + alpelisib
Vil^Cre
% initial area
Time (days)

Figure 4: Alpelisib impairs LIN28B-induced cell migration and invasion and inhibits PI3Kα-induced organoid growth. (A) Western blot analysis of pAKT (Ser473) and tAKT in CRC cells (one-way ANOVA, mean ± SEM). **(B)** Colony formation assay of LIN28B^{high} CRC cells treated with 5 μM alpelisib. Scale bars = 500 μm (one-way ANOVA, mean ± SEM). **(C)** Wound healing assay showing cell migration of CRC cells treated with 5 μM alpelisib at 0 hours. Scale bars = 500 μm (n=4; two-way ANOVA, mean ± SEM). **(D)** Transwell ECM invasion assay of CRC cells treated with 5 or 10 μM alpelisib. Scale bars = 1 mm (one-way ANOVA, mean ± SEM). **(E)** Representative brightfield images of colonic organoids derived from *Vil^{Cre}* mice treated with 5 μM alpelisib every 2 days for 5 days. Scale bars = 500 μm. **(F)** Western blot analysis of LIN28B, pAKT (Ser473), and tAKT in colonic organoids derived from *Vil^{Cre}* mice treated with 5 μM alpelisib (Student's unpaired t-test within each group, mean ± SEM). **(G)** Quantification of growth of colonic organoids derived from *Vil^{Cre}* mice treated with 5 μM alpelisib (n=3-5; two-way ANOVA, mean ± SEM; significance for day 5 shown with asterisks. The asterisk above datapoint signifies significance when compared to the *R26$^{WT/WT}$* control group).

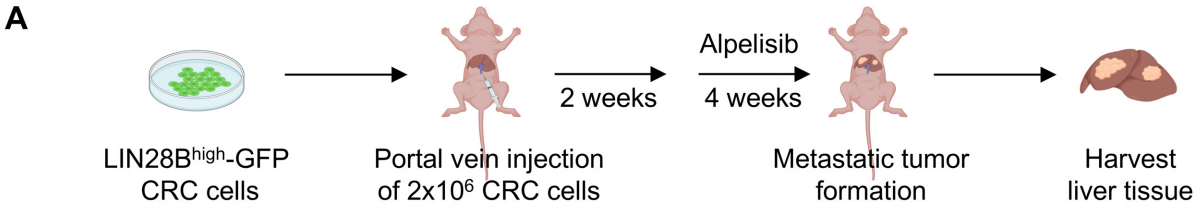
A
LIN28B^high-GFP CRC cells
Portal vein injection of 2x10^6 CRC cells
2 weeks
Alpelisib
4 weeks
Metastatic tumor formation
Harvest liver tissue

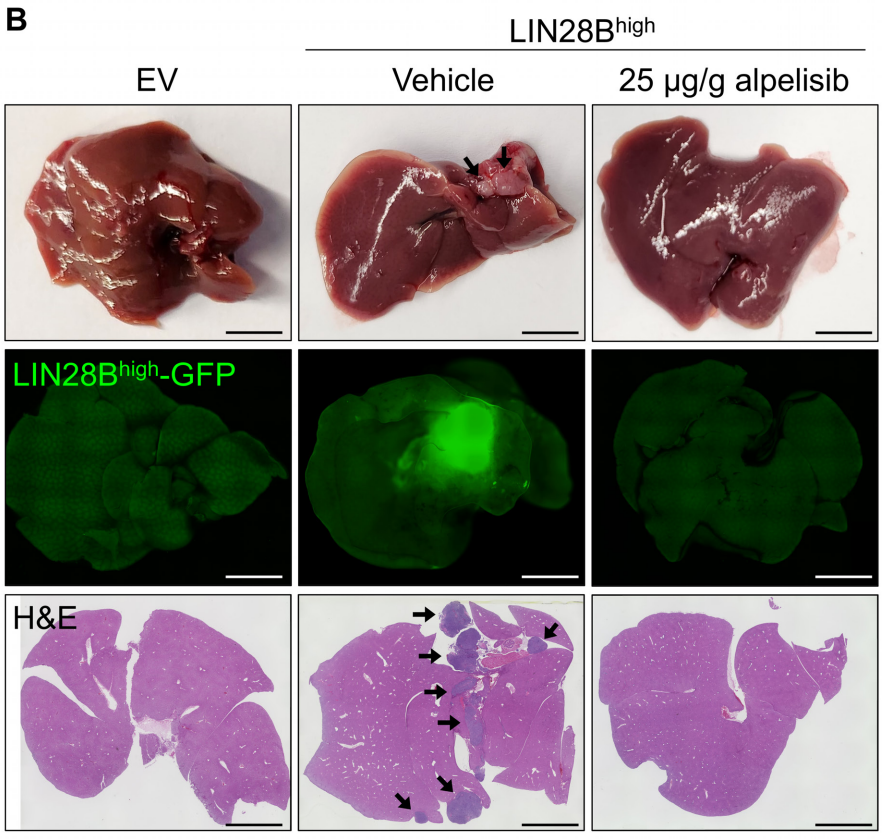
B
LIN28B^high
EV
Vehicle
25 µg/g alpelisib
LIN28B^high-GFP
H&E

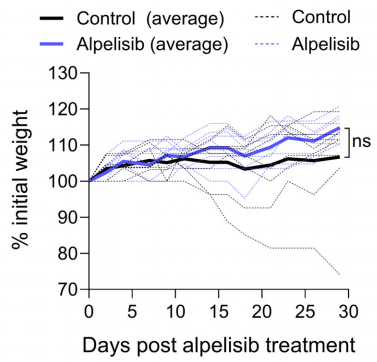
C
Control (average)
Alpelisib (average)
Control
Alpelisib
% initial weight
ns
Days post alpelisib treatment

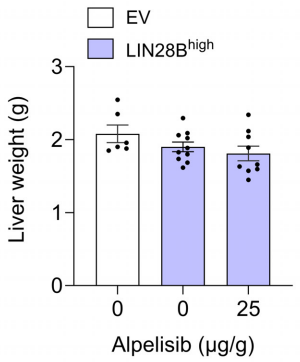
D
EV
LIN28B^high
Liver weight (g)
Alpelisib (µg/g)

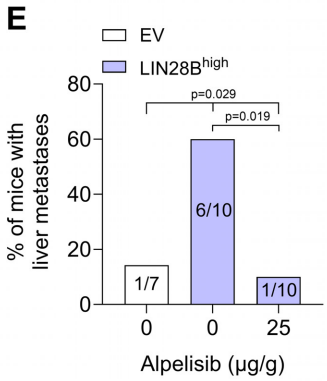
E
EV
LIN28B^high
% of mice with liver metastases
p=0.029
p=0.019
1/7
6/10
1/10
Alpelisib (µg/g)

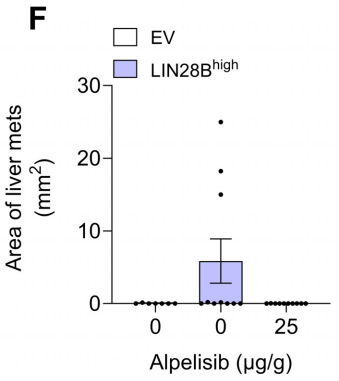
F
EV
LIN28B^high
Area of liver mets (mm^2)
Alpelisib (µg/g)

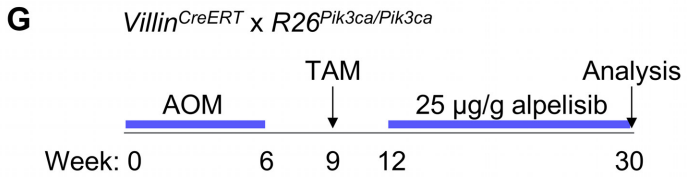
G
Villin^CreERT x R26^Pik3ca/Pik3ca
AOM
TAM
25 µg/g alpelisib
Analysis
Week: 0
6
9
12
30

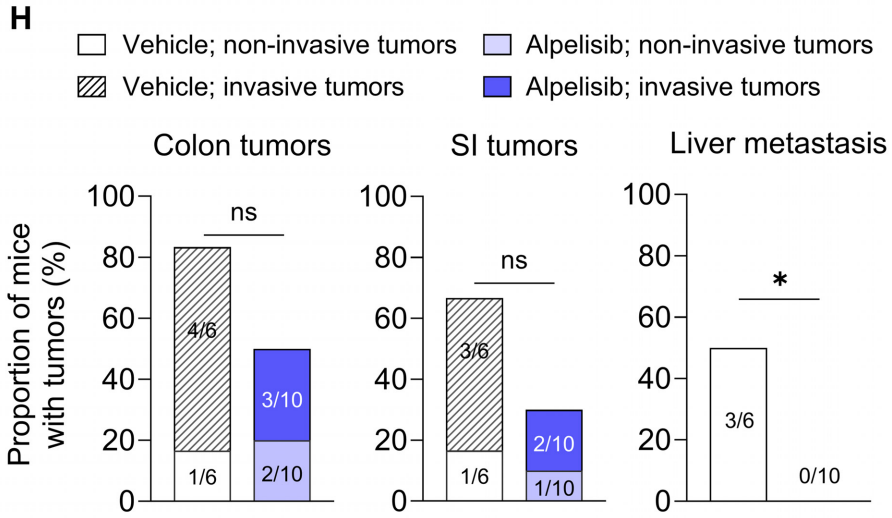
H
Vehicle; non-invasive tumors
Vehicle; invasive tumors
Alpelisib; non-invasive tumors
Alpelisib; invasive tumors
Colon tumors
SI tumors
Liver metastasis
Proportion of mice with tumors (%)
ns
ns
*
4/6
1/6
3/10
2/10
3/6
1/6
2/10
1/10
3/6
0/10

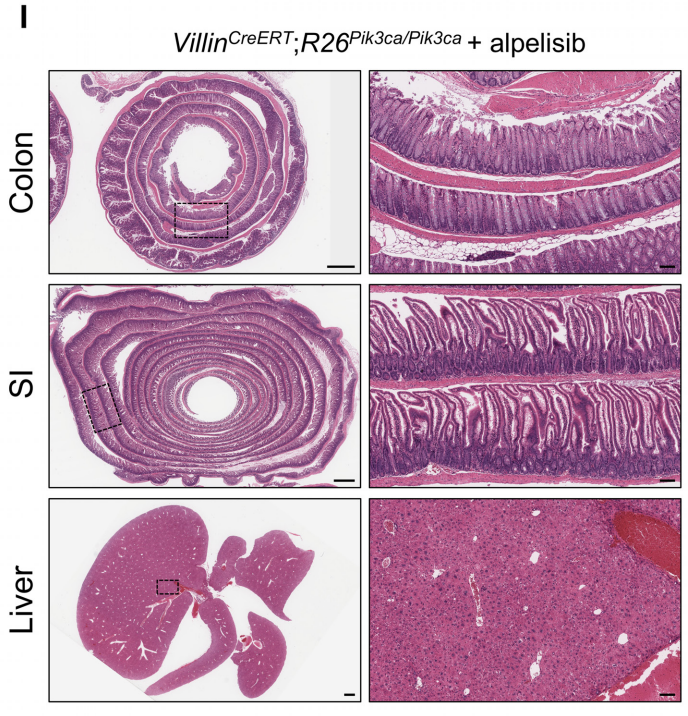
I
Villin^CreERT;R26^Pik3ca/Pik3ca + alpelisib
Colon
SI
Liver

Figure 5: Alpelisib inhibits colorectal liver metastasis formation in mice. (A) Experimental setup for investigating the effect of alpelisib on colorectal liver metastasis formation. **(B)** Representative images of liver tissues from mice injected with CRC cells and treated with vehicle or alpelisib. Gross liver morphology with black arrows denoting liver metastases (top), GFP fluorescence indicating liver metastases from LIN28B^{high}-GFP CRC cells (middle), and H&E staining with black arrows denoting liver metastases (bottom) are shown. Scale bars = 5 mm. **(C)** Weight change of mice over the course of the experiment, expressed as percentage of initial weight. Dotted lines = individual mice, solid line = average of all mice in group (n=7 and 10; ns, not significant). **(D)** Quantification of liver weight (one-way ANOVA, mean ± SEM). **(E)** Proportion of mice with liver metastases in each group (Chi-square test). The dataset for the control groups in this graph is the same as the data reported in Figure 1D. **(F)** Quantification of the area of liver metastases in each group (one-way ANOVA, mean ± SEM). **(G)** Experimental setup in which *Vil*^{CreERT}*;R26*$^{Pik3ca/Pik3ca}$ mice were treated with AOM to induce tumor formation, followed by tamoxifen, and subsequently treated with 25 μg/g alpelisib after primary tumors had formed. **(H)** Proportion of *Vil*^{CreERT}*;R26*$^{Pik3ca/Pik3ca}$ mice with tumors in the colon, SI, and liver metastases (Fisher's exact test; ns, not significant). **(I)** Representative H&E-stained images of colon, SI, and liver tissues from *Vil*^{CreERT}*;R26*$^{Pik3ca/Pik3ca}$ mice treated with alpelisib. Scale bars = 1 mm, scale bars for insets = 100 μm.

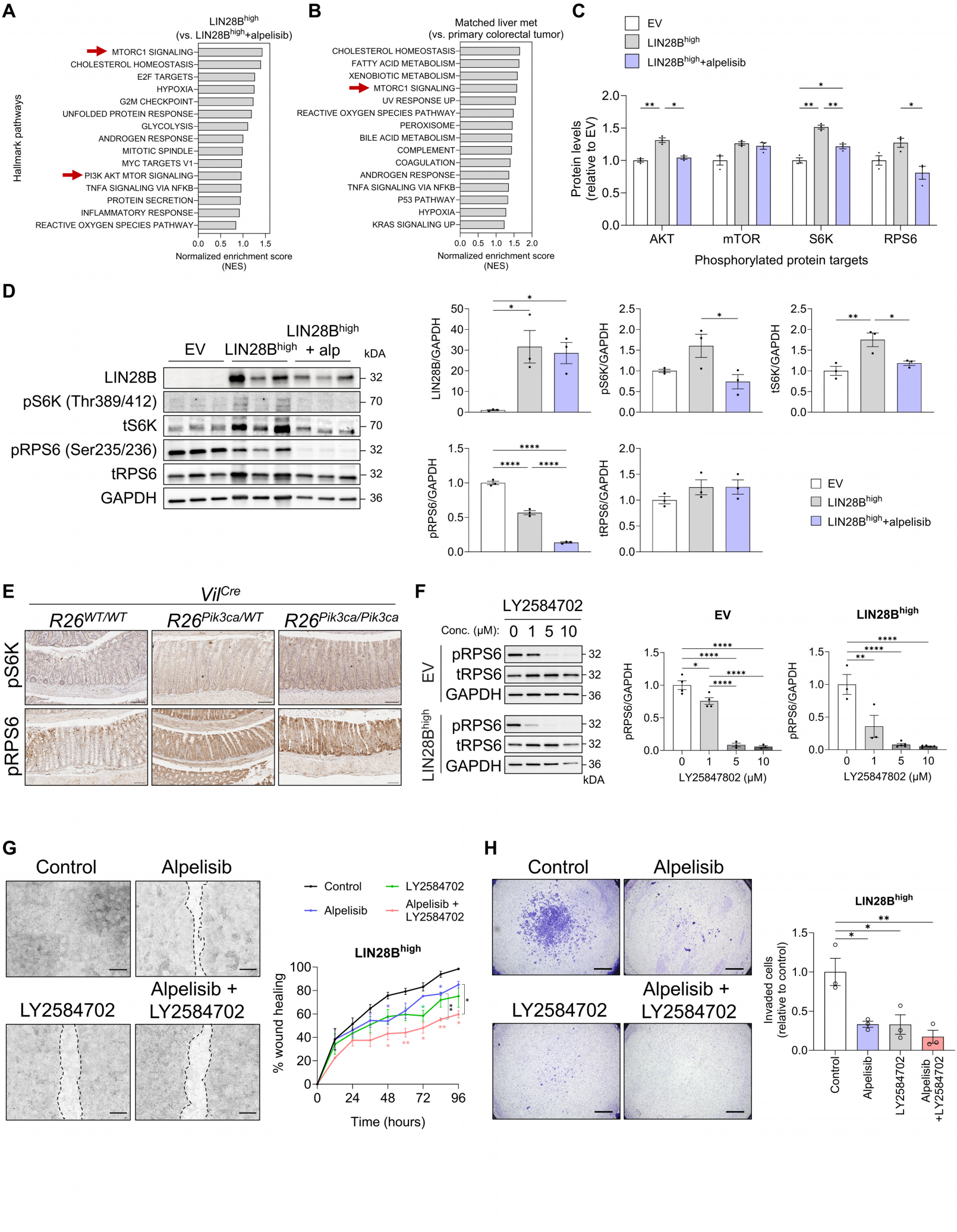
A
LIN28B^high
(vs. LIN28B^high+alpelisib)
MTORC1 SIGNALING
CHOLESTEROL HOMEOSTASIS
E2F TARGETS
HYPOXIA
G2M CHECKPOINT
UNFOLDED PROTEIN RESPONSE
GLYCOLYSIS
ANDROGEN RESPONSE
MITOTIC SPINDLE
MYC TARGETS V1
PI3K AKT MTOR SIGNALING
TNFA SIGNALING VIA NFKB
PROTEIN SECRETION
INFLAMMATORY RESPONSE
REACTIVE OXYGEN SPECIES PATHWAY
Hallmark pathways
Normalized enrichment score (NES)
B
Matched liver met
(vs. primary colorectal tumor)
CHOLESTEROL HOMEOSTASIS
FATTY ACID METABOLISM
XENOBIOTIC METABOLISM
MTORC1 SIGNALING
UV RESPONSE UP
REACTIVE OXYGEN SPECIES PATHWAY
PEROXISOME
BILE ACID METABOLISM
COMPLEMENT
COAGULATION
ANDROGEN RESPONSE
TNFA SIGNALING VIA NFKB
P53 PATHWAY
HYPOXIA
KRAS SIGNALING UP
Normalized enrichment score (NES)
C
EV
LIN28B^high
LIN28B^high+alpelisib
Protein levels (relative to EV)
AKT
mTOR
S6K
RPS6
Phosphorylated protein targets
D
LIN28B^high
EV
LIN28B^high
+ alp
kDA
LIN28B
pS6K (Thr389/412)
tS6K
pRPS6 (Ser235/236)
tRPS6
GAPDH
LIN28B/GAPDH
pS6K/GAPDH
tS6K/GAPDH
pRPS6/GAPDH
tRPS6/GAPDH
EV
LIN28B^high
LIN28B^high+alpelisib
E
Vil^Cre
R26^WT/WT
R26^Pik3ca/WT
R26^Pik3ca/Pik3ca
pS6K
pRPS6
F
LY2584702
Conc. (μM): 0 1 5 10
EV
LIN28B^high
pRPS6
tRPS6
GAPDH
kDA
EV
LIN28B^high
pRPS6/GAPDH
LY25847802 (μM)
G
Control
Alpelisib
LY2584702
Alpelisib + LY2584702
Control
Alpelisib
LY2584702
Alpelisib + LY2584702
LIN28B^high
% wound healing
Time (hours)
H
Control
Alpelisib
LY2584702
Alpelisib + LY2584702
LIN28B^high
Invaded cells (relative to control)
Control
Alpelisib
LY2584702
Alpelisib +LY2584702

Figure 6: Pharmacologic inhibition of the S6K/RPS6 axis suppresses LIN28B-driven cell migration and invasion in CRC cells. (A) GSEA from RNA-seq showing hallmark pathways enriched in LIN28B^{high} cells compared to LIN28B^{high} cells treated with 5 μM alpelisib. **(B)** GSEA from RNA-seq showing hallmark pathways enriched in liver metastasis compared to matched primary tumors in CRC patients (GSE50760). **(C)** Quantification of phosphorylated protein targets involved in the PI3K/AKT pathway in EV, LIN28B^{high}, and LIN28B^{high} cells treated with 5 μM alpelisib (one-way ANOVA for each protein target, mean ± SEM). **(D)** Western blot analysis of LIN28B, pAKT (Ser473), pS6K (Thr389/412), total S6K, pRPS6 (Ser235/236), tRPS6, and GAPDH in CRC cells treated with 5 μM alpelisib (alp, alpelisib; one-way ANOVA, mean ± SEM). **(E)** Representative IHC images of pS6K (Thr389/412) and pRPS6 (Ser235/236) in colonic tissues from *Villin*^{Cre} mice. Scale bars = 100 μm. **(F)** Western blot analysis of pRPS6, tRPS6, and GAPDH in CRC cells treated with varying concentrations of LY2584702 (S6K inhibitor) (one-way ANOVA, mean ± SEM). **(G)** Wound healing assay showing cell migration of LIN28B^{high} CRC cells (n=3; two-way ANOVA, mean ± SEM). **(H)** Transwell ECM invasion assay of LIN28B^{high} CRC cells (one-way ANOVA, mean ± SEM).

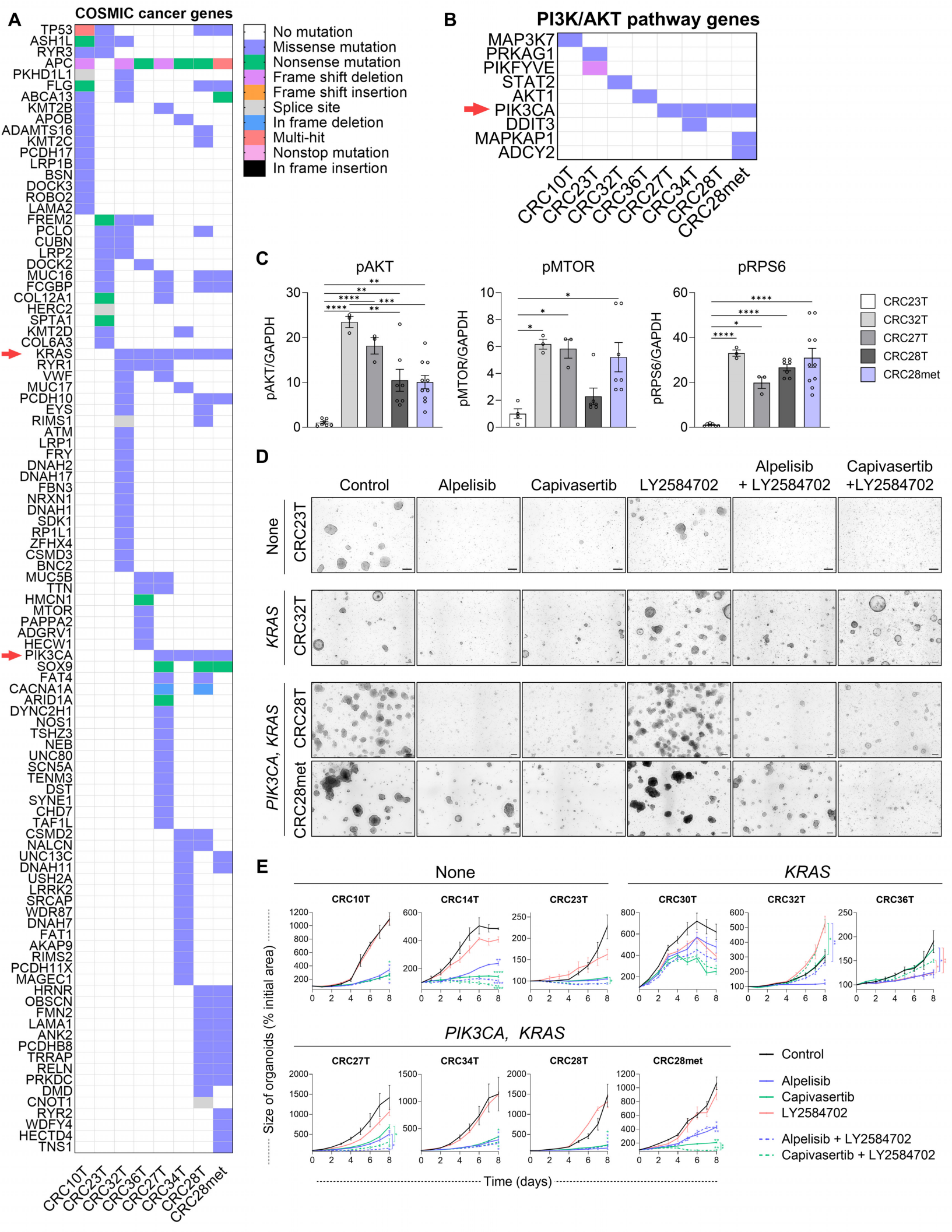
A
COSMIC cancer genes
No mutation
Missense mutation
Nonsense mutation
Frame shift deletion
Frame shift insertion
Splice site
In frame deletion
Multi-hit
Nonstop mutation
In frame insertion
TP53
ASH1L
RYR3
APC
PKHD1L1
FLG
ABCA13
KMT2B
APOB
ADAMTS16
KMT2C
PCDH17
LRP1B
BSN
DOCK3
ROBO2
LAMA2
FREM2
PCLO
CUBN
LRP2
DOCK2
MUC16
FCGBP
COL12A1
HERC2
SPTA1
KMT2D
COL6A3
KRAS
RYR1
VWF
MUC17
PCDH10
EYS
RIMS1
ATM
LRP1
FRY
DNAH2
DNAH17
FBN3
NRXN1
DNAH1
SDK1
RP1L1
ZFHX4
CSMD3
BNC2
MUC5B
TTN
HMCN1
MTOR
PAPPA2
ADGRV1
HECW1
PIK3CA
SOX9
FAT4
CACNA1A
ARID1A
DYNC2H1
NOS1
TSHZ3
NEB
UNC80
SCN5A
TENM3
DST
SYNE1
CHD7
TAF1L
CSMD2
NALCN
UNC13C
DNAH11
USH2A
LRRK2
SRCAP
WDR87
DNAH7
FAT1
AKAP9
RIMS2
PCDH11X
MAGEC1
HRNR
OBSCN
FMN2
LAMA1
ANK2
PCDHB8
TRRAP
RELN
PRKDC
DMD
CNOT1
RYR2
WDFY4
HECTD4
TNS1
CRC10T
CRC23T
CRC32T
CRC36T
CRC27T
CRC34T
CRC28T
CRC28met
B
PI3K/AKT pathway genes
MAP3K7
PRKAG1
PIKFYVE
STAT2
AKT1
PIK3CA
DDIT3
MAPKAP1
ADCY2
CRC10T
CRC23T
CRC32T
CRC36T
CRC27T
CRC34T
CRC28T
CRC28met
C
pAKT
pMTOR
pRPS6
pAKT/GAPDH
pMTOR/GAPDH
pRPS6/GAPDH
CRC23T
CRC32T
CRC27T
CRC28T
CRC28met
D
Control
Alpelisib
Capivasertib
LY2584702
Alpelisib + LY2584702
Capivasertib +LY2584702
None
CRC23T
KRAS
CRC32T
PIK3CA, KRAS
CRC28T
CRC28met
E
None
KRAS
PIK3CA, KRAS
CRC10T
CRC14T
CRC23T
CRC30T
CRC32T
CRC36T
CRC27T
CRC34T
CRC28T
CRC28met
Size of organoids (% initial area)
Time (days)
Control
Alpelisib
Capivasertib
LY2584702
Alpelisib + LY2584702
Capivasertib + LY2584702

Figure 7: Pharmacologic inhibition of PI3Kα and S6K impairs the growth of CRC PDOs. (A) Heatmap showing top 200 CRC mutations in Catalogue of Somatic Mutations in Cancer (COSMIC) cancer genes in PDO lines identified by WES. Only genes with mutations are shown. Mutation types are color-coded as indicated in the legend (T, primary tumor; met, liver metastasis). **(B)** Heatmap showing mutations in PI3K/AKT pathway genes in PDO lines identified by WES. Refer to the list of PI3K/AKT pathway genes used in Supplemental Methods. Only genes with mutations are shown. **(C)** Quantification of Western blot analysis of pAKT (Ser473), phosphorylated mTOR (pMTOR) (Ser2448), and pRPS6 (Ser235/236) in PDO lines (one-way ANOVA, mean ± SEM). **(D** and **E)** Representative bright-field images (D) and growth curves (E) of PDOs treated with the inhibitors every other day for 8 days. Scale bars = 100 μm. (n=3; two-way ANOVA, mean ± SEM).

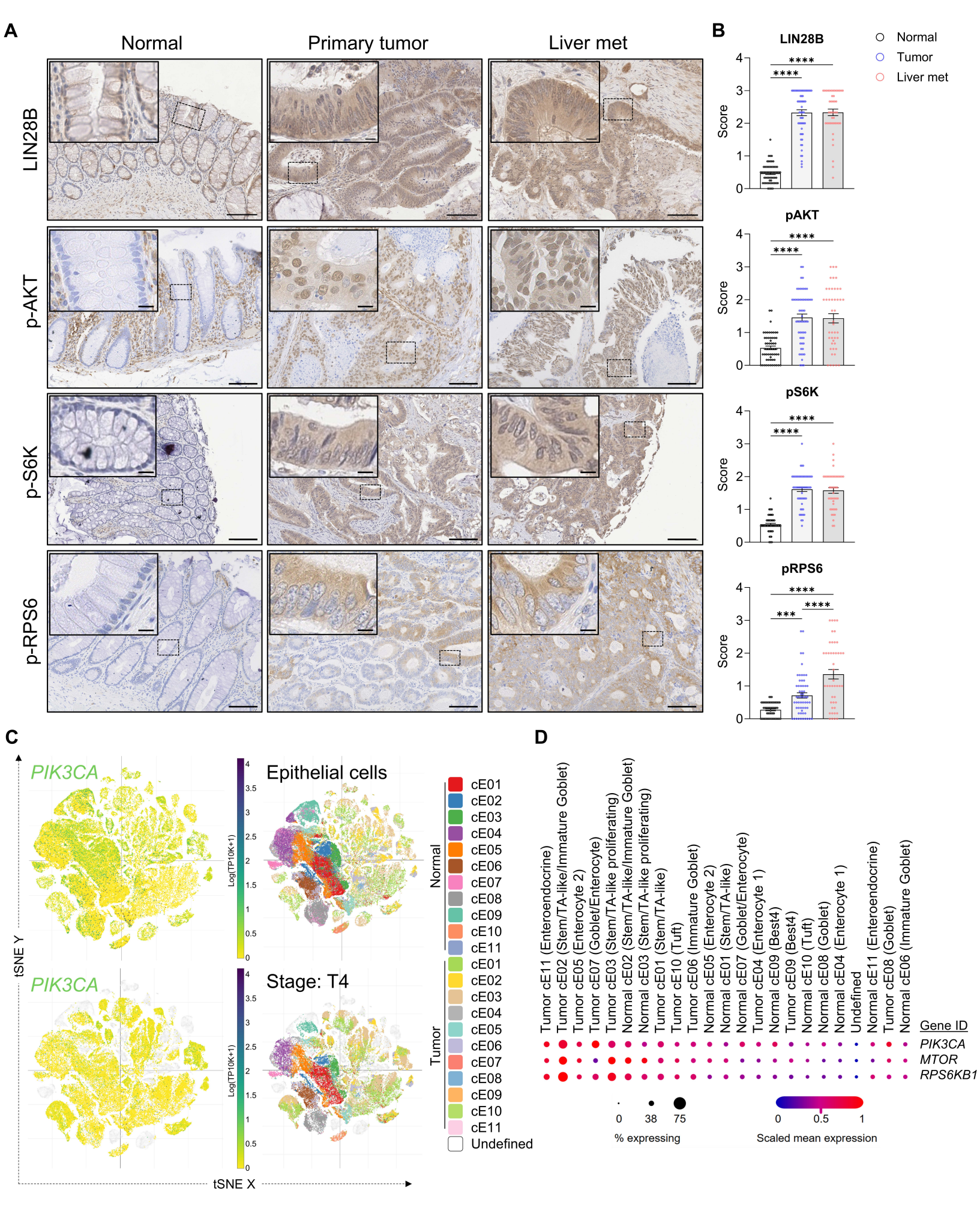
A
Normal
Primary tumor
Liver met
LIN28B
p-AKT
p-S6K
p-RPS6
B
Normal
Tumor
Liver met
LIN28B
pAKT
pS6K
pRPS6
Score
****
***
C
PIK3CA
Log(TP10K+1)
Epithelial cells
Stage: T4
tSNE Y
tSNE X
Normal
Tumor
cE01
cE02
cE03
cE04
cE05
cE06
cE07
cE08
cE09
cE10
cE11
Undefined
D
Tumor cE11 (Enteroendocrine)
Tumor cE02 (Stem/TA-like/Immature Goblet)
Tumor cE05 (Enterocyte 2)
Tumor cE07 (Goblet/Enterocyte)
Tumor cE03 (Stem/TA-like proliferating)
Normal cE02 (Stem/TA-like/Immature Goblet)
Normal cE03 (Stem/TA-like proliferating)
Tumor cE01 (Stem/TA-like)
Tumor cE10 (Tuft)
Tumor cE06 (Immature Goblet)
Normal cE05 (Enterocyte 2)
Normal cE01 (Stem/TA-like)
Normal cE07 (Goblet/Enterocyte)
Tumor cE04 (Enterocyte 1)
Normal cE09 (Best4)
Tumor cE09 (Best4)
Normal cE10 (Tuft)
Normal cE08 (Goblet)
Normal cE04 (Enterocyte 1)
Undefined
Normal cE11 (Enteroendocrine)
Tumor cE08 (Goblet)
Normal cE06 (Immature Goblet)
Gene ID
PIK3CA
MTOR
RPS6KB1
% expressing
Scaled mean expression

Figure 8: PI3K-S6K signaling correlates with disease progression in CRC patient samples. **(A)** Representative IHC images of LIN28B, pAKT (Ser473), pS6K (Thr389/412), and pRPS6 (Ser235/236) in normal adjacent colon tissue, primary colon tumor, and liver metastases from 60 CRC patients. Scale bars = 100 μm, scale bars for insets = 10 μm. **(B)** Quantification of IHC staining scores for LIN28B, pAKT, pS6K, and pRPS6 (n=60; one-way ANOVA, mean ± SEM). **(C)** t-SNE plots showing the expression of *PIK3CA* in all epithelial cells (above) and in T4 stage tumor cells (below) from the Human Colon Cancer Atlas single-cell sequencing dataset (c295) comprising 371,223 cells. **(D)** Dot plot showing scaled mean expression and percentage of cells expressing *PIK3CA*, *MTOR*, and *RPS6KB1* across different cell clusters (normal colonic epithelial and tumor cells) identified in the Human Colon Cancer Atlas dataset (cE, colonic epithelium).

TABLES

Table 1: Patient demographics and tumor characteristics used for generation of PDOs.

PDO line	Age	Sex	Pathology	Location	Differentiation status	Stage	Neoadj. therapy	MSI-H	Common mutations (CSTP)
CRC10	58	M	Adenocarcinoma	Descending	Well	pT2N0	No	No	None
CRC14	44	F	Adenocarcinoma	Descending	Moderate	pT2N2a	No	No	None
CRC23	81	F	Adenocarcinoma	Ascending	Moderate	pT4aN2b	No	No	None
CRC30	64	F	Adenocarcinoma	Ascending	Moderate	pT2N0	No	No	*KRAS (G12D)*
CRC32	43	F	Adenocarcinoma	Rectum	Moderate-poor	pT4bN0M1	Yes	No	*KRAS (G13D)*
CRC36	85	F	Adenocarcinoma	Ascending	Moderate	pT3N0	No	No	*KRAS (G12D)*
CRC27	64	F	Adenocarcinoma	Ascending	Moderate	pT4aN1a	No	No	*PIK3CA (E545K)* *KRAS (G12D)*
CRC28	73	M	Adenocarcinoma	Ascending	Moderate	pT3N1aM1a	No	No	*PIK3CA (E545K)* *KRAS (G12V)*
CRC34	75	F	Adenocarcinoma	Transverse	Moderate	pT3N0	No	No	*PIK3CA (Q546E)* *KRAS (G12D)*

Information on the patient demographics and tumor characteristics for the PDO lines used in the study. Neoadj., neoadjuvant; MSI-H, microsatellite instability-high; CSTP, Columbia Solid Tumor Panel.

Table 2: The Colorectal/Pancreatic Subpanel within Columbia Solid Tumor Panel (CSTP) consisting of clinically actionable genes.

Gene Name	Mutations (Exons)
BRAF	NM_004333 e11,15
ERBB2	NM_004448 e8,17,19-21
FBXW7	NM_033632 e5,7-12
GNAQ	NM_002072 e2,4,5
GNA11	NM_002067 e4-5
KRAS	NM_004985 e2-4
NRAS	NM_002524 e2-4
PIK3CA	NM_006218 e2,3,5,7,8,10,14,19,21
POLD1	NM_002691 e4-10,15-20,24
POLE	NM_006231 e1,2,9,11,13,14,20,21,25,26
STK11	NM_000455 e1-9, full coding sequence

List of clinically actionable genes included in the colorectal and pancreatic subpanel of the Columbia Solid Tumor Panel that were used for tumor tissues collected for PDO generation.